BRAIN SOURCE LOCALIZATION IN THE PRESENCE OF LEADFIELD PERTURBATIONS

by

Rabiya Nakhat Momin

A Thesis Presented to the Faculty of the
American University of Sharjah
College of Engineering
in Partial Fulfillment
of the Requirements
for the Degree of

Master of Science in
Electrical Engineering

Sharjah, United Arab Emirates

May 2015

Approval Signatures

We, the undersigned, approve the Master's Thesis of Rabiya Nakhat Momin

Thesis Title: Brain Source Localization in the Presence of Leadfield Perturbations.

Signature	**Date of Signature** (dd/mm/yyyy)
_____	_____
Dr. Hasan Mir Associate Professor of Electrical Engineering Thesis Advisor	
_____	_____
Dr. Hasan Al-Nashash Professor of Electrical Engineering Thesis Advisor	
_____	_____
Dr. Nasser Qaddoumi Professor of Electrical Engineering Thesis Committee Member	
_____	_____
Dr. Ibrahim Kamel Professor of Electrical Engineering University of Sharjah Thesis Committee Member	
_____	_____
Dr. Nasser Qaddoumi Head of Department of Electrical Engineering	
_____	_____
Dr. Mohamed El-Tarhuni Associate Dean of College of Engineering	
_____	_____
Dr. Leland Blank Dean of College of Engineering	
_____	_____
Dr. Khaled Assaleh Interim Vice Provost for Research and Graduate Studies	

Acknowledgments

First and foremost I thank Allah (S.W.T) for helping me accomplish what I had set out to do.

Then, I would like to express my deepest gratitude to all the people that helped me and under whose direction and support I was able to achieve the final outcomes of this thesis.

I would like to thank my advisors; Dr. Hasan Mir, for his guidance and persistent help throughout the course of this thesis and Dr. Hasan Al-Nashash, for his constant encouragement, support and suggestions. I am greatly indebted to the both of you. I would also like to acknowledge Ms. Tahereh Zarghami for her insightful comments and assistance.

I am also grateful to my sister Sabah, as well as my friends Minna and Ayah, for their witty comments, constructive criticism and positive reassurances. A special mention to my friends Sonia and Pallavi for being there with me through thick and thin. I love and admire each one of you in perhaps unhealthy amounts.

Thank you to my lovely parents for keeping me sane and understanding me when I couldn’t understand myself, and my dear cat Cassy for providing me with comfort, albeit unknowingly.

Lastly, I am thankful and fortunate enough to receive assistance as well as the opportunity to enhance my learning from the Department of Electrical Engineering at the American University of Sharjah.

To the ever growing curiosity of the human mind…

Abstract

Brain source localization enables us to localize different areas of the brain that are activated during any mental activity. This thesis makes use of Electroencephalography (EEG) recordings which is an important noninvasive tool for studying the temporal dynamics of the human brain. EEG source localization finds its applications in cognitive neuroscience in order to develop a Brain Computer Interface (BCI), and in psychopharmacology and psychiatry, to localize sources in certain frequency bands. Unfortunately, EEG readings cannot directly indicate the location of the source of brain activity using the signals measured on the scalp, which contributes to the ambiguity of the *inverse problem*. In order to solve the ill-posed inverse problem, array processing methods are implemented, in conjunction with various techniques that are applied, to improve the localization in the presence of calibration errors. In this thesis, a recently developed G-MUSIC algorithm is applied to the problem of brain source localization. G-MUSIC is a form of weighted MUSIC that performs better in scenarios where only limited sample support is available. Two transfer function based calibration algorithms are also developed to estimate the accurate location of neural activity in the brain when the measured leadfield is perturbed. The localization performance of G-MUSIC is compared to the traditional MUSIC algorithm and quantified in terms of the localization error. This thesis also addresses the problem of localization when exact knowledge of the leadfield matrix, for an individual head anatomy, is not available, by developing an iterative algorithm. This algorithm includes a high resolution localization technique, recently used in radar field, called Source Affine Image Reconstruction Algorithm (SAFFIRE) that can determine the model order (number of sources) and their locations. A beamformer is then designed in order to estimate the dipole source amplitudes. Finally, the EEG signal is reconstructed and related to the actual EEG signal via a calibration matrix. This procedure is repeated until a convergence criteria is met. The performance of this algorithm is quantified in terms of the localization error and accuracy and further validated by applying it to experimental data. In conclusion, the algorithm is also tested on non-stationary EEG signal, where a variant of the conventional adaptive beamformer is applied in order to estimate the source signal amplitudes.

Search Terms: ***Brain source localization, EEG, inverse problem, calibration, BEM.***

Table of Contents

List of Figures

List of Tables

List of Abbreviations

ABF	-	Adaptive Beamformer
DOA	-	Direction of Arrival
BEM	-	Boundary Element Method
EEG	-	Electroencephalography
FFA	-	Fusiform Face Area
MRI	-	Magnetic Resonance Imaging
MSE	-	Mean Square Error
MUSIC	-	Multiple Signal Classification Algorithm
MVB	-	Minimum Variance Beamformer
RISR	-	Reiterative Super-Resolution Algorithm
SAFFIRE	-	Source Affine Image Reconstruction Algorithm
SNR	-	Signal to Noise Ratio
TBF	-	Taylor Series Beamformer

Chapter 1: Introduction

1.1 Brain Source Localization

Neuroimaging techniques are increasingly becoming important in both research and healthcare. These techniques help in understanding the relationship between specific areas of the brain and the functions they serve. Neuroimaging is also used to identify neural networks that are involved in cognitive processes and in localizing different regions that are activated in the brain. This research makes use of electroencephalography (EEG) readings. Fundamentally, EEG is a noninvasive technique that measures electric potentials due to any neural activity in the brain. Due to its low hardware costs and high temporal resolution, EEG provides a complement to neuroimaging techniques, such as positron emission tomography (PET) and functional magnetic resonance imaging (fMRI). Moreover, EEG offers the possibility of measuring neuronal activity in real time, as needed, when investigating the temporal properties of the brain [1]. Clinically, EEG is used in the diagnosis of neurological disorder, such as epilepsy and sleep disorders. In cognitive neuroscience, EEG source imaging is used to analyze event related potentials (ERP) in order to improve the performance of Brain-Computer Interface machines (BCI).

In order to perform EEG source localization, we must first solve the *forward problem*. Forward problem makes use of appropriate volume conductor head models in order to obtain electric fields outside the scalp, as a result of neural activity. Neurons, that produce these electric fields, are modeled as current dipoles for which a mathematical model is developed. This mathematical model approximates the primary current density that represents the source of brain activity to be localized.

However, the signals measured on the surface of the scalp, do not directly indicate the location of the activated neuron. This is mainly because various source configurations produce the same measured electric fields on the surface of the scalp. Consequently, the only way to localize putative electric sources in the brain is by making a-priori assumptions on the generation of EEG signals, this is known as the *inverse problem*. The bio electromagnetic inverse problem consists of localizing the source of signals collected in response to neural activity. In order to solve the inverse problem, array processing methods are used and various techniques are implemented

to improve source localization error in the presence of calibration errors. These methods and calibration techniques are discussed in detail in Chapters 4, 5 and 6.

1.2 Problem Statement

Array processing methods provide a robust signal processing tool to solve the inverse problem. Multiple Signal Classification (MUSIC) is a well-known subspace-based source localization algorithm that utilizes the eigen structure of the spatial covariance matrix and provides a computationally efficient alternative to maximum likelihood (ML) algorithms [2]. Improved localization accuracy is afforded through the use of more electrodes; this in turn requires more time samples in order to obtain an accurate estimate of the data covariance matrix. However, enough time samples may not be available or usable due to the nonstationarity property of the signal. Nonstationarity could arise due to different time scales involved in the dynamical process, which for EEG waves is on the order of 10 milliseconds whereas that of an action potential is about 1 millisecond [3].

In cases where only a limited number of samples are available, the performance of the MUSIC algorithm degrades, since part of the energy from the noise subspace of the covariance matrix leaks into the signal subspace, causing the two subspaces to lose their orthogonality. In order to counter this problem, a new source localization technique called G-MUSIC is proposed in [4] which is a form of weighted MUSIC. Furthermore, various anomalies can cause the measured leadfield to differ from the theoretical leadfield. These anomalies can arise due to e.g. co-registration and approximation of the head model, with limited accuracy and discretization of the source space, and are termed as calibration errors [5]. As such, array calibration is required to account for any discrepancies that may cause the actual leadfield to differ from the theoretical one [6]. This thesis develops a combined calibration and localization framework for EEG systems operating in the limited sample regime.

Another challenge encountered in brain source localization is estimating an accurate forward problem solution, known as the leadfield matrix. In order to obtain an accurate solution, a precise volume conductor head model is required. Although modeling realistic head conductors, using techniques such as finite element method (FEM) and boundary element method (BEM), improve localization accuracy, they are deemed impractical when incorporated as a part of an iterative solution, due to the high

computational complexity that accompanies creating the leadfield matrix. Furthermore, employing a pre-determined realistic head model, or a simple single sphere head model, may not suffice due to various forward problem uncertainties, such as different conductivity profile or the volume shape of an individual.

Therefore, an iterative algorithm is developed in this thesis to address the problem of localization without having the exact knowledge of the leadfield matrix for an individual anatomy.

1.3 Thesis Methodology and Outline

In this thesis, the forward problem solution is obtained using a software called Brainstorm. The assumption made in this software is that the brain's neural activity is modeled as a current dipole and is placed normal to the surface of the cortex. Furthermore, various volume conductor models are available in this software in order to model the head, of which two head models, the three shell sphere head model and the realistic head model, are used in this thesis. In the entire thesis a BioSemi 64 electrode system is used that is based on the actual device available in the market. Next, small regions of interest on the cortex are considered to be active and specific source waveforms are assigned to them. Using the source and head models synthetic EEG signals are then generated for the purpose of localization.

Firstly, a high resolution subspace based localization algorithm, that can localize sources even when limited time samples are available, is investigated. This algorithm called G-MUSIC is derived from G-estimation techniques and is compared with the conventional MUSIC algorithm [4]. Unlike MUSIC which only uses eigenvectors from the noise subspace, G-MUSIC uses all (signal and noise) eigenvectors of the data covariance matrix and therefore, is able to accurately localize sources even when finite time samples are available. Additionally, two calibration techniques have been implemented in order to improve localization accuracy in the presence of forward model uncertainties, denoted as calibration errors. The performance of the calibration techniques, coupled with G- MUSIC, is assessed and compared against the traditional MUSIC algorithm in terms of the source localization error.

Next, an iterative algorithm is developed in order to estimate the location and amplitudes of the sources of neural activity, even when exact knowledge of the leadfield

matrix for an individual head anatomy is not available. This algorithm includes, (1) high resolution localization algorithm originally used in the radar field, in order to determine the number of sources and their locations; (2) a beamformer, in order to determine the source amplitudes; and (3) a calibration technique, in order to relate the actual received EEG signal and the EEG signal reconstructed using the algorithm. The performance of the iterative algorithm is quantified, in terms of the localization error, before and after calibrating the system. Finally, this algorithm is applied to real data in order to localize sources of neural activity based on the experiment, as well as to determine the shape of the source waveform.

The rest of the thesis is organized as follows:

Chapter 2 provides information on the brain's anatomy and physiology that is required to understand the topic. Moreover, EEG is introduced and compared to other functional neuroimaging techniques on the basis of spatial and temporal resolution.

Chapter 3 outlines the modeling of the bio electromagnetic fields. The forward problem is formally introduced in this chapter. Maxwell's equations are reviewed and the quasi-static approximation of the equations is derived for this application. Also, various head models that effect localization accuracy, are discussed in this chapter.

Chapter 4 includes the literature review done on various existing signal processing techniques used to solve the inverse problem. Two general approaches, called the parametric and imaging techniques, are introduced and prominent examples of each technique are reviewed. The advantages and drawbacks of each of these techniques are also briefly mentioned in this chapter.

Chapter 5 introduces the principles of array processing methods. Two subspace based localization algorithms are compared in this chapter. Additionally, two calibration techniques are implemented in order to improve the localization accuracy in the presence of calibration errors. The performance of the subspace based methods, coupled with the calibration techniques, is quantified in terms of the MSE and localization error.

Chapter 6 presents the iterative algorithm developed in order to localize sources and determine their amplitudes. This chapter also introduces a high resolution phased array technique and mentions its advantages over SCM based techniques stated in

Chapter 5. The performance of the iterative algorithm is assessed in this chapter in terms of the localization error.

Chapter 7 investigates the performance of the iterative algorithm developed in the previous chapter on experimental data.

In Chapter 8 the proposed algorithm is applied to a non-stationary EEG signal. Moreover, a new source amplitude estimation technique is introduced.

Chapter 9 includes the conclusion and some recommendations regarding future work.

Chapter 2: Brain Anatomy and Physiology

2.1 The Human Brain

The brain is considered as the most complex part of the human body. From an anatomical point of view, the brain can be divided into three parts: the cerebrum, cerebellum and the brain stem. All parts of the brain work together, however each part has its own special function. The cerebellum coordinates the movement of muscles and maintains balance whereas the brain stem controls respiration, hormone secretion, etc. Situated at the topmost part of the brain, the cerebrum is responsible for our intellectual activities. The cerebrum is split into the right hemisphere and the left hemisphere with a deep furrow separating the two [7]. The outermost layer of the cerebrum is defined as the *cerebral cortex*, also referred to as grey matter, consisting mainly of cell bodies in contrast to the white matter that consists of axons [8].

2.1.1 Cerebral Cortex. The cortex is the most important part of the central nervous system responsible for higher order functions, such as processing sensory information and is involved in decision making and problem solving processes. The human cortex is 2-4 mm thick and is deeply wrinkled, which makes the brain more efficient as it increases the surface area of the brain and the amount of neurons it contains [8]. The cortex can be divided into four lobes as shown in Fig.1, based on their different functionalities, namely (1) the frontal lobe associated with planning, reasoning and emotions; (2) the parietal lobe responsible for perception of stimuli, recognition and movement; (3) the occipital lobe related to visual processing and; (4) the temporal lobe associated with recognition and perception of auditory stimuli, speech and memory [9].

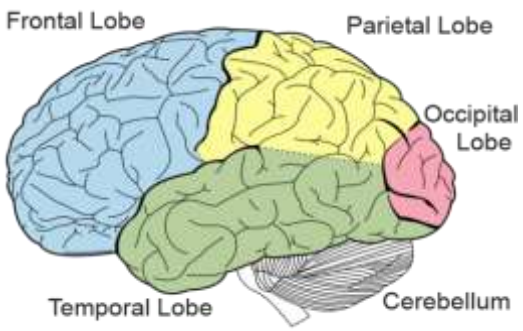

Figure 1: The cerebral cortex [10]

The majority of the cortex is represented by the neocortex which consists of six layers labelled from outer to inner as I to VI. The six horizontal layers of the neocortex are separated on the basis of cell type and neuronal connections. Layers III and V predominantly consist of the *pyramidal neurons* that are pyramidal in shape and the apical dendrite of which extends to layer I of the cortex. Moreover, the axons of pyramidal cells extend to distant brain regions in contrast with stellate cells that are most prominent in layer IV and the axons of which remain within the cortex [8].

2.1.2 Neurons: The Origin of Electric Signals. Current flow is produced within the brain due to the activation of the fundamental unit of the brain, neurons. Each neuron in the brain influences and is influenced by other neurons, communicating with each other using chemical and electrical signals. Neurons are composed of the dendrites, cell body (soma), axon and the myelin as indicated in Fig.2 [8].

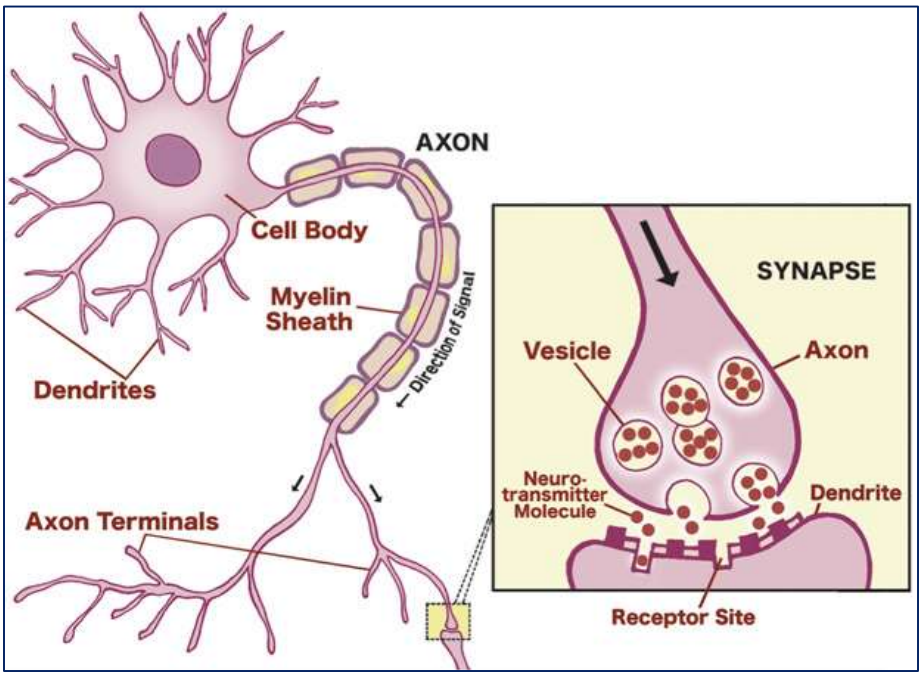

Figure 2: Components of a neuron and communication between neurons (inset) [11]

In order to communicate, the dendrites accumulate information from other neurons. The cell body then integrates the received information and produces an electric signal called the *action potential*. This action potential then propagates in the axon and releases chemical signals called neurotransmitters into the synaptic cleft. These neurotransmitters diffuse across the synapse and latch onto the receptors located on the

target neuron. The signal received by the target neuron may increase its membrane potential exciting it, in such a case, it is referred to as an excitatory post synaptic potential (EPSP). On the other hand, the received signal may decrease the membrane potential of the target neuron inhibiting it, therefore it is referred to as inhibitory post synaptic potential (IPSP). This process, continues as long as the membrane potential of the neuron exceeds a certain excitation threshold, producing the action potential, described in Fig.3 [12].

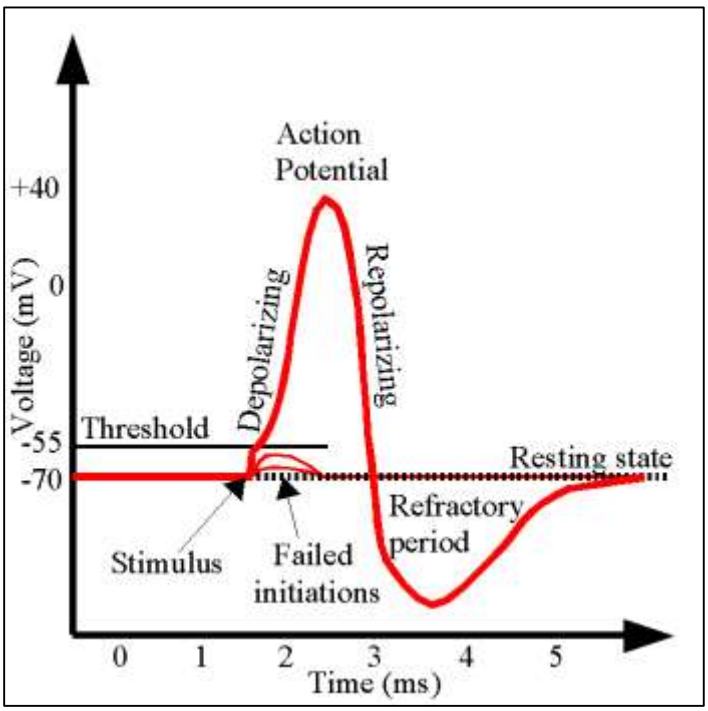

Figure 3: Neuron Action Potential [13]

2.1.3 Electrochemical Reactions in the Neuron. Neurons have a membrane which is selectively permeable to ions. The concentration of ions, such as K^+, Na^+, and Cl^-, is different inside the cell than it is outside. In its resting state, a neuron has a membrane potential of around -70mV, with respect to the outside of the cell. The negative potential is due to the outflow of K^+ ions, which gives rise to a shortage of positive charges inside the membrane [12]. Once the cell is excited in response to a stimulus, the permeability of ions is altered. Na^+ channels open allowing a small influx of Na^+ ions inside the cell. This inflow of Na^+ ions increases the membrane potential such that it exceeds the threshold voltage i.e. -55mV and an action potential is fired. As a result, more Na^+ ions flood in, causing the membrane potential to be positive.

Subsequently, the K^+ channels open and allow K^+ ions to flow outside the cell at some positive membrane potential. As the Na^+ channel closes stopping the inflow of positive charge, the K^+ channel continues the outflow of the positive charge, as a result of which the membrane potential plunges, ultimately bringing the membrane to its resting state [12].

As a particular section of the axon undergoes the process outlined above, it increases the membrane potential of the next section in the axon, provoking a similar action potential. This chain reaction, illustrated in Fig.4, makes sure that the action potential propagates only in one direction along the axon. Furthermore, when depolarization begins at one end of the neuron, the other end repolarizes back to -70mV, thus creating a dipole conducting current [8].

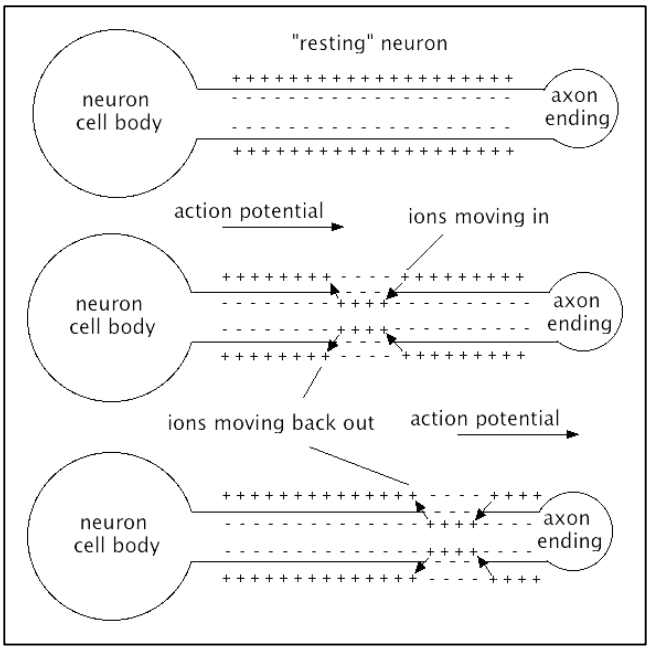

Figure 4: Propagation of action potential along the axon [14]

2.2 Electroencephalography (EEG)

EEG is a functional brain imaging technique that records the brain's spontaneous electrical activity. EEG measures the potential differences between pairs of scalp electrodes. The EEG electrodes are directly glued to the skin, at selected locations above cortical regions that are of interest. The electrodes are normally fitted in an elastic cap for uniform coverage of the scalp [15]. EEG is mainly used as a diagnostic test for epilepsy and other brain disorders.

2.2.1 Neurophysiological Basis of EEG. The postsynaptic potential, mentioned in Section 2.1.2, can be represented by a current dipole giving rise to *intracellular* or *primary* currents produced within the dendrites. These currents exist for several tens of milliseconds creating an electric field over the scalp [8]. In addition to intracellular currents, the conservation of electric charges imposes that the current loop must be closed with *extracellular* or *secondary (volume)* currents. The generation of the primary and secondary currents is shown in Fig.5.

However, a single EPSP produces a current dipole along the dendrite with a strength of 20fAm, which is too small to be measured by EEG systems. EEG systems record dipoles with a strength of 10nAm, therefore a cumulative summation of one million synaptic junctions in a small cortical region is required [15].

An EEG signal, therefore, is a measurement of currents flowing in the volume conductor due to the synaptic excitation of dendrites in pyramidal neurons. Due to the spatially structured arrangement of cells, pyramidal cortical neurons are considered to be the main contributors to EEG signals. Moreover, the EPSP generated in their dendrites tend to last longer than the rapidly moving action potentials traveling along the axons of excited neurons [15].

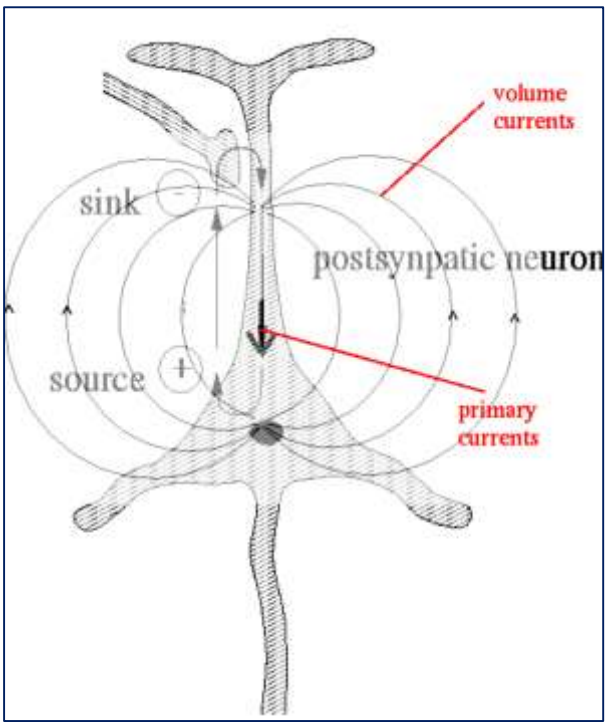

Figure 5: Generation of primary and secondary currents in a postsynaptic neuron [16]

2.2.2 Advantages and Limitations of EEG. EEG is a noninvasive technique with low hardware cost and high temporal resolution on the order of milliseconds as compared to functional magnetic resonance imaging (fMRI) and positron emission tomography technique (PET) that have a temporal resolution between seconds and minutes [17]. Moreover, EEG offers the possibility of measuring neuronal activity in real time, as needed, when investigating temporal properties of the brain. Furthermore, EEG measures brain's electrical activity directly, while the other methods such as PET and fMRI, record changes in blood flow or metabolic activity, which are indirect markers of brain's electrical activity.

Poor spatial resolution is one of the main disadvantages of EEG. Essentially the measurements taken at the scalp is the sum of electric fields produced by a large population of neurons. The spatial resolution of each electrode is on the order of one centimeter of the cortex, which encapsulates thousands of neurons [18]. As a result strong electrical activity can be detected by the neighboring electrodes as well. Thus, the exact source of activity using EEG signals is hard to pinpoint.

Chapter 3: Forward Problem

3.1 Generation of Bio Electromagnetic Fields

The development of mathematical techniques in order to examine the spatiotemporal activities in the brain, is required to analyze EEG measurements. As mentioned earlier, the *inverse problem* involves estimation of the current sources from which neural activity originates. However, before such an estimation is made, the *forward problem* must be solved. Solving the forward problem entails computing scalp potentials for a specific set of neural characteristics. Fig.6. shows a schematic of the current dipole as a source of neural activity inside the brain.

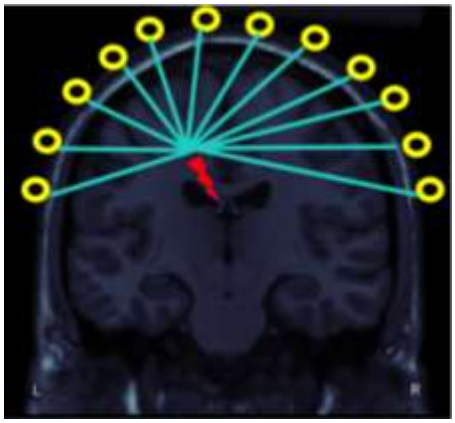

Figure 6: Electrical activity in a neuron is modeled as a current dipole. The electric fields corresponding to synchronous neural activity is detected by EEG electrodes placed on the scalp

Mathematically, the forward problem can be modeled as, [19]

$$V_{ij} = \int L_{ij}^{M}(r) \,.\, J^{P}(r)\, dV \tag{1}$$

Here, V_{ij} denotes the potential difference measured between electrodes *i* and *j*. $L_{ij}^{M}(r)$ is the leadfield for electrode pairs i and j and depends on the location and configuration of the electrodes and is expressed in Ω/m. $J^{P}(r)$ represents the primary current density emanating from a source at location *r* and is expressed in A/m^2. In order to solve the forward problem, unique solutions for the electric potentials can be obtained, as long as the approximated leadfields (L) and primary current densities $J^{P}(r)$ are known. Since a unique solution can be formulated, the forward problem is considered to be well posed. On the contrary, solving the inverse problem requires the measured potentials (V) and approximated leadfields (L) in order to detect the position of the primary current densities $J^{P}(r)$. Since, the solution consists of many different

possibilities, the inverse problem is said to be ill-posed. Therefore, in order to solve the inverse problem accurately, modeling of the forward problem is required.

3.2 Quasi-static Approximation of Maxwell's Equations

The famous Maxwell equations for electric field *E* are [20]:

$$\nabla \times \boldsymbol{E} = -\frac{\partial \boldsymbol{B}}{\partial t} \tag{2}$$

$$\nabla \times \boldsymbol{H} = \frac{\partial \boldsymbol{D}}{\partial t} + \boldsymbol{J} \tag{3}$$

where $\boldsymbol{E}$ is the electric field intensity (V/m), $\boldsymbol{B}$ is the magnetic flux density (W/m^2), $\boldsymbol{D}$ is the electric flux density (C/m^2) and $\boldsymbol{H}$ is the magnetic field intensity (A/m). Further, the constitutive relations between the electric field quantities are defined as follows:

$$\boldsymbol{D} = \in \boldsymbol{E} \tag{4}$$

$$\boldsymbol{J} = \sigma \boldsymbol{E} \tag{5}$$

where the constitutive parameters $\in$ and σ correspond to the permittivity (F/m) and conductivity (S/m) of the medium. For EEG signals, the useful frequency spectrum is found to be below 1 kHz. As a result, we can apply a quasi-static approximation to the Maxwell equations by eliminating the terms with time dependency. Therefore, (2) can be rewritten as:

$$\nabla \times \boldsymbol{E} = 0 \tag{6}$$

Next, taking divergence on both sides of (3) will result in,

$$\nabla.(\nabla \times \boldsymbol{H}) = \nabla.\boldsymbol{J} \tag{7}$$

We get the left hand side of (7) to be,

$$\nabla.\boldsymbol{J} = 0 \tag{8}$$

The total current density $\boldsymbol{J}$ that is produced by neuronal activity in the brain is denoted as,

$$\mathbf{J} = \boldsymbol{J}_p + \boldsymbol{J}_\Omega \tag{9}$$

where $\boldsymbol{J}_p$ represents the primary current generated by neural activity in neuronal cells and $\boldsymbol{J}_\Omega$ represents the volume/secondary currents that flow passively in the conductive

medium. The source of brain activity that needs to be located is characterized by the primary current density $\boldsymbol{J_p}$**.** Nevertheless, modeling the volume currents improves the localization accuracy.

3.3 Current Dipole as a Source

As mentioned in Section 2.2, when the axon of a presynaptic neuron synapse with the basal dendrites of a postsynaptic pyramidal neuron, it may induce an excitatory post synaptic potential. As a result, the sodium channels open allowing an influx of sodium (Na^+) ions into the axon. As depolarization begins at one end of the neuron, the other end repolarizes back to the resting potential i.e. – 70 mV, thus creating a current dipole and conducting current. The dipole model is valid when neuronal activity is dominated by a small brain area.

Consider a small patch of activated cortex where a current dipole $\boldsymbol{Q}$ at $\boldsymbol{r_Q}$ can be considered as a concentration of $\boldsymbol{J_p}(\boldsymbol{r})$ to a single point [19]:

$$\boldsymbol{J_p}(\boldsymbol{r}) = \boldsymbol{Q}\ \delta(\boldsymbol{r} - \boldsymbol{r_Q}) \tag{10}$$

where, $\delta(r)$ is the Dirac delta function**.** The forward problem mainly involves calculating the potential (V) on the scalp from a given primary current distribution within the brain. Hence, (6) can be satisfied by representing $\boldsymbol{E}$ as

$$\boldsymbol{E} = -\nabla V \tag{11}$$

Using (5) the volume current can be represented as,

$$\boldsymbol{J_\Omega} = \sigma \boldsymbol{E} \tag{12}$$

$$\boldsymbol{J_\Omega} = -\sigma \nabla V \tag{13}$$

From (9) we obtain,

$$\mathbf{J} = \boldsymbol{J_p} - \sigma \nabla V \tag{14}$$

Also, from (8) it is clear that $\nabla . \boldsymbol{J} = 0$. Applying divergence on both sides we get,

$$\nabla . (\sigma \nabla V) = \nabla . \boldsymbol{J_p} \tag{15}$$

The above equation can be solved for V either numerically implementing finite element techniques, or analytically in special cases, by using appropriate boundary conditions [19].

3.4 Head Models

An accurate head model is required to solve the inverse problem. The head model determines the way sources located within the brain produce measurements on the scalp. It essentially includes the geometrical (shape, symmetry) and electromagnetic (permeability and conductivity) properties of the volume and are mathematically expressed in the leadfield matrix.

As mentioned in equation (1), in order to calculate the forward solution which is the scalp potential, the leadfield is multiplied with the current density vector i.e. the estimated sources. The distance between the measured potentials and those predicted using (1) is the basis for locating the sources [1].

3.4.1 Single Sphere Model. The most simple, and often used head model, is the single sphere head model [1]. Since this head model assumes uniform conductivity, an analytical solution is fast and easy to calculate.

Nonetheless, source localization accuracy is found to be limited for a single sphere head model and inadequate when considering certain regions of the brain, for example the frontal and frontal-temporal areas [5]. Also, the head, in reality, is not necessarily spherical and homogenous and therefore, the assumption made regarding the conductivity does not suffice.

3.4.2 Multiple Spheres Head Model. An extension of the single sphere head model is the multiple spheres head model illustrated in Fig.7, which consists of multiple spheres to represent layers with different conductivities.

The three layer concentric shell head model assumes concentric, homogenous spherical shells representing the scalp, skull and the brain and is considered to be a viable head model due to the simplicity with which the head parameters are characterized and the availability of rapidly computable closed form expressions [8].

This model is used in most clinical and research applications related to EEG source localization and compared to the single sphere head model ameliorates the localization accuracy to a certain extent.

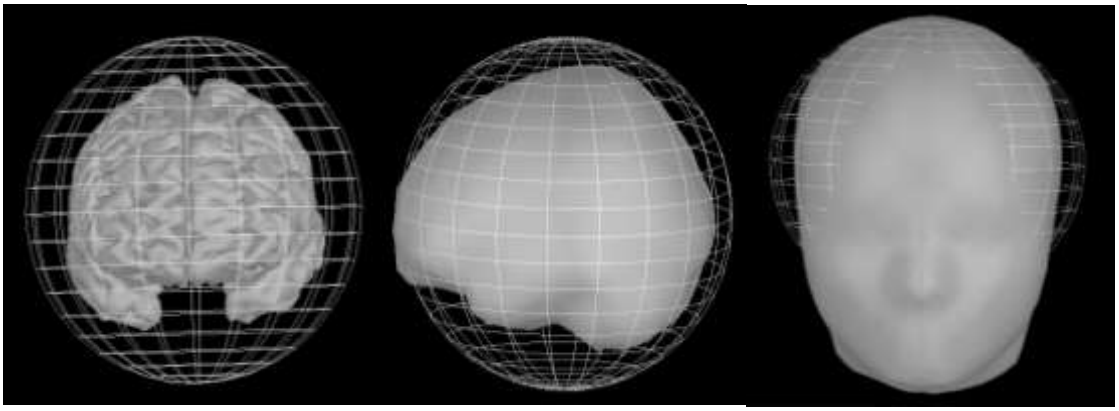

Figure 7: Three layer concentric head model, homogenous spheres representing the cortex, skull and the scalp

3.4.3 Realistic Head Model. Accurate leadfield computations with high localization accuracy for anisotropic, inhomogeneous and non-spherical heads can only be achieved by using realistic volume conductor models. Boundary element method (BEM) and finite element method (FEM) are the most popular techniques used for realistic head modeling.

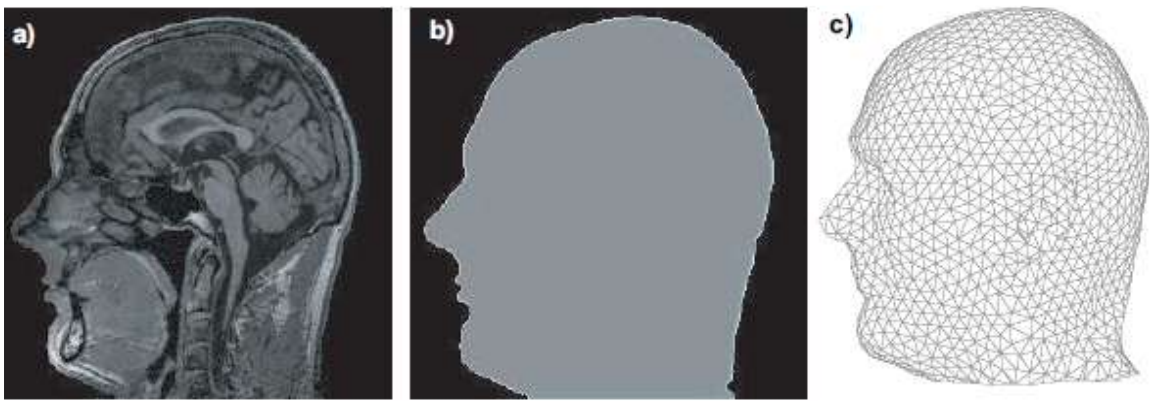

Figure 8: Modeling of a realistic head model using BEM [8]

BEM replaces the true surfaces with planar triangles as indicated in Fig.8. However, BEM assumes homogeneity and isotropy within each region of the head. FEM on the contrary, tessellates the entire volume and takes into account the individual anisotropic conductivities for each element.

Nevertheless, the generation of realistic geometric head models is not a trivial task and the computations are very intensive. This method is impractical when incorporated as a part of an iterative inverse solution and may take a long time to converge. Even though the issue regarding computational load is increasingly becoming irrelevant, studies have reported that the differences between spherical and realistic

head models in the case of a single dipole localization decrease with increasing noise in the data [1]. A tessellated FEM head model is shown in Fig.9.

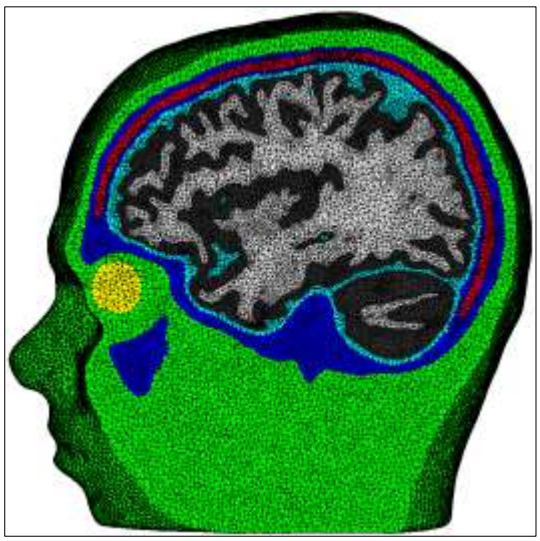

Figure 9: Realistic FEM head model [21]

Chapter 4: Inverse Problem

The inverse problem involves locating the sources of neural activity in the brain using the set of potentials obtained by solving the forward problem. In this chapter, various existing signal processing based techniques that are used to solve the bio electromagnetic inverse problem are studied. Two general approaches, known as parametric and imaging techniques, are used for the estimation of EEG source locations and amplitudes [15]. The concept behind the two approaches, along with the assumptions made and their inherent limitations, will be discussed in this chapter.

4.1 Parametric modeling

The main assumption made in parametric methods is that the sources can be represented by a few equivalent current dipoles where the locations, amplitudes and orientations of these dipoles can be estimated with a non-linear numerical method.

4.1.1 Least Squares Source Estimation. The focal sources of neural activity are modeled as equivalent current dipoles in this method where six parameters are assigned to each dipole. The six parameters are, (1) three location parameters (x, y, z); (2) two orientation parameters (elevation and azimuth angles); (3) one amplitude (strength) parameter.

In this method, the number of dipoles and their initial parameters are first selected. Next, the resulting electric potentials, i.e. forward solution, is computed for the provided dipole parameters. Later, the computed electric potentials are compared to the actual electric potentials by calculating the squared error (square of the Frobenius norm) between the two [15], [22].

A non-linear search algorithm is usually applied iteratively in order to minimize the squared error over all dipole parameters. The main goal of the algorithm is to determine the dipole parameters that best explain the measured electric potentials [22]. This process is carried on until some minimization criteria is satisfied.

The least squares approach can be applied to various dipole models, the three most widely used models are the fixed dipole model, the moving dipole model and the rotating dipole model. When the dipole strength is estimated keeping the orientation and position constant within a given interval, it is referred to as the *fixed dipole model*. Further, when the least squares model is applied sequentially to each time interval,

allowing all the parameters of the dipole to vary, the result is called the *moving dipole model*, since the location is not fixed. The *rotating dipole model* allows the orientations and the strengths of the dipole to vary, however, the position of the dipole is constrained to one point. These dipole models are very widely used with most EEG clinical and experimental data [15].

One of the main drawbacks of the least squares approach is that the exact number of dipole sources are often not known a-priori and hence must be determined by the user before applying the algorithm.

Furthermore, as the number of dipoles sources increases, chances of being trapped in the local minima increases due to the nonconvexity of the least squares cost function. Therefore, we will discuss some other alternative methods that avoid the problem of nonconvexity by scanning a particular region of interest. Beamforming and multiple signal classification techniques are some alternative methods that avoid non-convexity, and in some cases can determine the number of underlying sources. An estimator based on the contribution of each putative source location to the data can be derived using either spatial filtering or signal classification indices [15].

4.1.2 Beamforming. Originally, beamforming is a radar and sonar technique that has found its applications in many other research fields, such as astronomy and biomedical signal processing. Essentially, a beamformer performs spatial filtering on the data received from a sensor array in order to discriminate between signals originating from a location of interest and those originating from elsewhere [15].

However, there are insufficient degrees of freedom and therefore a strong stop band constraint cannot be placed over the entire brain region. Thus, a fixed spatial filter is not practical for this application. An alternative adaptive technique called, linearly constrained minimum variance beamforming (LCMV), is implemented that uses a limited number of degrees of freedom to place nulls in the response at positions corresponding to unwanted, interfering sources. By minimizing the output power, nulling is achieved and a unity gain constraint is applied at the desired location.

One of the main limitations of the LCMV method is partial signal cancellation due to the fact that neural activity in different regions of the brain is often found to be correlated [15]. Nevertheless, recent studies suggest that the LCMV method can tolerate

moderate amounts of source or interference correlation. Mainly, beamformers perform well when then are only few independent components present in the data that are not strongly correlated.

Another disadvantage of the LCMV method is that any errors in the leadfield matrix (forward solution) can result in attenuation, or worse, cancellation of signals, therefore, more elaborate constraints must be designed. However, as the number of constraints increases, the number of degrees of freedom reduces, as a result of which the beamformer becomes less adaptive to other unknown sources [15].

4.1.3 MUSIC. The Multiple Signal Classification method (MUSIC) was first used in array signal processing before being used as a localization technique for EEG signals. In this technique, eigen decomposition is used in order to decompose the data covariance matrix into the signal and noise subspace. Sources are assumed to be located at positions where the forward solution is orthogonal to the noise subspace [15].

Similar to beamforming techniques, MUSIC assumes that the signals are discrete, uncorrelated and fewer in number than the sensors, moreover the noise is assumed to be white. Further, this method may be difficult to implement on online data, since the partitioning of the data into signal and noise subspace is more easily performed on averaged data [23].

MUSIC, and its variant called G-MUSIC, are discussed in further detail as localization techniques in the next chapter.

4.2 Imaging (Non-Parametric methods)

Imaging, or non-parametric methods, are based on the assumption that the primary sources generating the EEG signals are intracellular currents flowing in the dendritic trunks of the cortical pyramidal neurons. As mentioned earlier, these neurons are aligned normal to the surface of the cortex. Further, the cortex surface is tessellated into thousands of elements, where a dipole is assumed at each of the tessellations with its orientation constrained to be normal to the local surface [15]. As such, the inverse problem is considered to be linear, since the unknowns in this problem are only the amplitudes of the dipoles placed at each tessellation.

However, since the number of sensors is on the order of 100 and the number of unknowns is about 15,000, the problem is ill-posed and therefore regularization

methods are implemented in order to limit the number of solutions. Some of the methods and their limitations are described in the sections below.

4.2.1 Bayesian Method. The Bayesian approach is a statistical technique that incorporates a-priori information regarding the anatomy of the head and brain, smoothness etc. in order to determine the variance and expectation of the a-posteriori probability of the source current [1].

Assume that we have to estimate a matrix of dipole amplitudes $\boldsymbol{S}$, placed at each tessellation element from a spatio-temporal data matrix $\boldsymbol{M}$, which in the noiseless case can be described as [15]:

$$\boldsymbol{M} = \boldsymbol{A}\boldsymbol{S}^T \tag{16}$$

where, $\boldsymbol{A}$ is the forward problem solution and the i^{th} row of $\boldsymbol{S}$ corresponds to the amplitude image across the cortex at time instant *i*. Then, applying the Bayes theorem we obtain the posterior probability as [15]:

$$p(\boldsymbol{S}|\boldsymbol{M}) = \frac{p(\boldsymbol{M}|\boldsymbol{S})\, p(\boldsymbol{S})}{p(\boldsymbol{M})} \tag{17}$$

where, $p(\boldsymbol{M}|\boldsymbol{S})$ is the conditional probability for the data given the image and $p(\boldsymbol{S})$ is based on our knowledge of the statistical properties of the unknown image and is denoted as the prior distribution. Further, images are estimated by the maximization of the log-posterior probability [15]:

$$\widehat{\boldsymbol{S}} = arg\max_{S} ln\, p(\boldsymbol{M}|\boldsymbol{S}) + ln\, p(\boldsymbol{S}) \tag{18}$$

where, $p(\boldsymbol{M}|\boldsymbol{S})$ is the log likelihood of the data and depends on the forward model and true current source distribution. Nevertheless, the noiseless scenario considered in this approach is not realistic since EEG data is assumed to be corrupted with additive white Gaussian noise. Then, the log likelihood is given as [15]:

$$lnp(\boldsymbol{M}|\boldsymbol{S}) = \frac{1}{2\sigma^2}||\boldsymbol{M} - \boldsymbol{A}\boldsymbol{S}^T||^2{}_F \tag{19}$$

Next, for the prior probability an exponential distribution function is assumed [15]:

$$p(\boldsymbol{S}) = \frac{1}{z}\, e^{-\beta\, f(\boldsymbol{S})} \tag{20}$$

where, z and β are scalar constants and $f(\boldsymbol{S})$ is a function of the image $\boldsymbol{S}$. By combining the log likelihood and the log prior, the general form of the negative log posterior is obtained whose minimization yields the maximum a posteriori estimate [15]:

$$U(\boldsymbol{S}) = ||\boldsymbol{M} - \boldsymbol{A}\boldsymbol{S}^T||^2 + \lambda\, f(\boldsymbol{S}) \tag{21}$$

where, $\lambda = 2\beta\sigma^2$.

In the Bayesian approach, several physiological assumptions are made in order to reduce the solution space a-priori. Some of these assumptions are: (1) sources must be located in the gray matter; (2) sources are placed perpendicular to the cortical surface; and (3) sources must be locally coherent. Anatomical information gathered from magnetic resonance imaging (MRI) can be used to impose the first two conditions. Additionally, the third condition can be enforced by minimizing the distance between neighboring voxels (spatial smoothness) [22]. Moreover, by determining the orientation of the dipoles a-priori, the inverse problem reduces from a vectorial problem of determining amplitudes and orientations to a scalar problem of determining dipole source amplitudes [22]. The rest of the imaging methods discussed below are special cases of minimization of the energy function described in (21).

4.2.3 Linear Imaging Methods. As mentioned earlier, in order to solve the ill-posed inverse problem, imaging methods make use of regularization techniques or some prior. Therefore, (21) can be interpreted as a Tikhonov regularized method of the inverse problem. The first term in the equation can be viewed as a measure of the fit to the data and the second term measures the smoothness of the function, as is referred to as the regularization function [15]. The scalar regularization parameter λ can be chosen using cross validation techniques and the L-curve [15]. Further information regarding the Tikhonov technique can be found in [24], [25].

Several forms of linear imaging techniques have been proposed for the purpose of EEG source localization, one of the first ones being the minimum norm (MN) solution [15]. The head model, in this technique, is mapped to a 3-D grid, and at each grid point, three mutually perpendicular dipole currents are assumed. The aim of this

technique is to determine the amplitudes and distribution of thousands of dipoles, such that they minimize the overall current density in the brain [22].

However, a disadvantage of the MN technique is its tendency to favor weak and localized activation patterns, especially those closer to the surface of the cortex. Additionally, the MN approach has low spatial resolution (blurring) due to the ill-posed nature of the EEG inverse problem. As a result, various weighting factors have been suggested to compensate for the shortcoming of the MN approach, one of them being the weighted MN solution. The weighted MN solution makes use of leadfield normalization in order to account for the lower representation of sources located deep into the brain. A second technique, called Focal Undetermined System Solution (FOCUSS), reduces the weights of the grid points with the lowest current density iteratively until the current density at most grid points is zero [22].

Low Resolution Electromagnetic Tomography (LORETA) is another famous MN based approach that introduces a spatial second derivative (Laplacian) into the weighting function. Essentially, LORETA minimizes the Laplacian of the sources and picks the solution with the smoothest spatial distribution [22]. Similar to the Bayesian technique, the solution space in LORETA is constrained to the gray matter of the cortex. Moreover, due to the smoothness required, this method has low spatial resolution.

Chapter 5: Source Localization using Subspace Based Methods with Low Sample Support

5.1 Principles of Array Signal Processing

Using sensors arranged in different patterns, array signal processing helps detect signals and determine information about them. In order to understand the concept a uniform linear array is considered due to its simplistic geometry. For the sake of simplicity the far field assumption is made, where the signals received by the electrodes behave like plane waves and are parallel to each other.

5.1.1 Uniform Linear Array (ULA). Consider a uniform linear array consisting of *M* sensors that are a distance *d* apart from each other as shown in Fig.10. The impinging signal is assumed to be in the far field so that it can be considered as a planar wave. The distance covered by the wave to reach each sensor in the array is different. As a result the signal received by each sensor will be a phase shifted replica of each other.

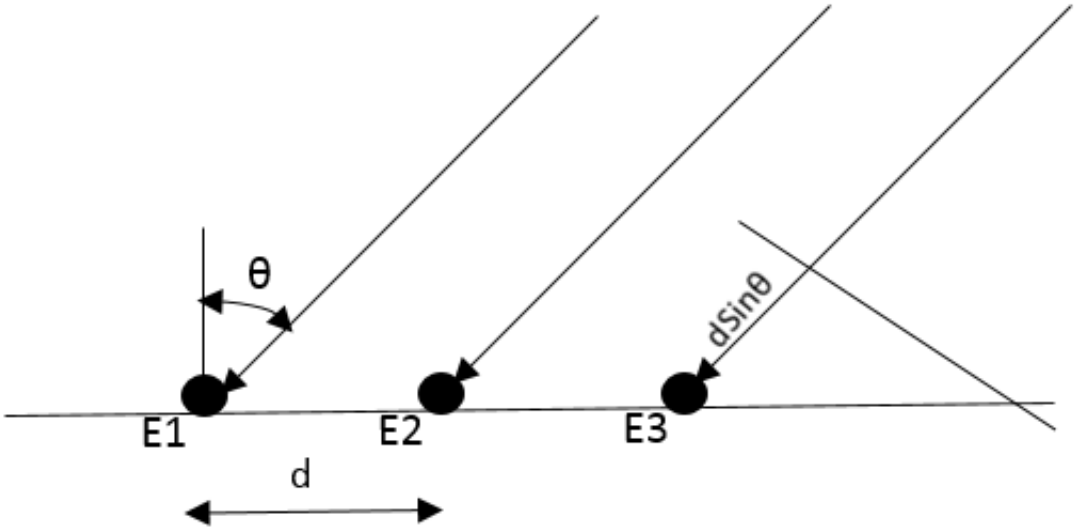

Figure 10: Uniform linear array of sensors

For a far field geometrical model, we consider the following expression [26]:

$$\Delta\tau_i = \frac{i\, dSin\theta}{c} \qquad ;\ i = 1,2,\dots\dots,M \tag{22}$$

where, $\Delta\tau_i$ is the time delay of the signal received by the sensor *i* with respect to the first sensor and *c* is the speed of light.

Assuming the signal is narrowband and removing the random initial phase term of the signal via IQ demodulation, the n[th] sample of the i[th] sensor is denoted as [26]:

$$y_i[n] = x[n]e^{-j2\pi\, f_c\, \Delta\tau_i} \tag{23}$$

where f_c is the center frequency of the narrowband signal. The Nyquist equivalent of the sampling rate in order to avoid spatial aliasing is [27]:

$$d \leq \frac{\lambda_{min}}{2} \tag{24}$$

where λ_{min} is the minimum wavelength corresponding to the maximum frequency. Therefore, the distance between any two sensors must be less than or equal to half the minimum wavelength.

Consequently, from (22), (24) and substituting $c = \lambda f_c$ we get,

$$y_i[n] = x[n]e^{-j\pi\, nSin\theta} = x[n]\, s_i(\theta) \tag{25}$$

Accounting for all array elements in the presence of *K* signal sources and additive Gaussian noise $v_i[n]$ we can represent (25) in matrix form as:

$$\begin{bmatrix} y_1[n] \\ y_2[n] \\ . \\ . \\ y_M[n] \end{bmatrix} = \begin{bmatrix} s_1(\theta_1) & \cdots & s_1(\theta_K) \\ \vdots & \ddots & \vdots \\ s_M(\theta_1) & \cdots & s_M(\theta_K) \end{bmatrix} \begin{bmatrix} x_1[n] \\ x_2[n] \\ . \\ . \\ x_K[n] \end{bmatrix} + \begin{bmatrix} v_1[n] \\ v_2[n] \\ . \\ . \\ v_M[n] \end{bmatrix} \tag{26}$$

5.2 Signal Model

In a more compact form for *N* time samples (26) can be rewritten as:

$$\boldsymbol{y}(n) = \boldsymbol{S}\boldsymbol{x}(n) + \boldsymbol{v}(n) \tag{27}$$

here, $\boldsymbol{S}$ is a normalized *M* x *K* leadfield matrix, $\boldsymbol{x}(n)$ is a *K* x 1 source vector and $\boldsymbol{v}(n)$ is a *K* x 1 zero mean additive Gaussian noise vector at time sample *n*.

Each column of the leadfield matrix $\boldsymbol{S}$ is referred to as the steering vector of the *K* signal sources. If the angles of arrivals of each of the *K* signals is different, the steering vectors are considered to be linearly independent and thus can be used to find

the corresponding angles. In order to compute the spatial covariance matrix, we assume that the signal vector $\boldsymbol{x}(n)$ and the noise vector $\boldsymbol{v}(n)$ are uncorrelated. Furthermore, we assume that the different elements of the noise vector are uncorrelated. Then, the true M x M spatial covariance matrix of the observation can be represented as:

$$\boldsymbol{R} = E[\boldsymbol{y}(n)\boldsymbol{y}(n)^H] = E[(\boldsymbol{S}\boldsymbol{x}(n) + \boldsymbol{v}(n))(\boldsymbol{S}\boldsymbol{x}(n) + \boldsymbol{v}(n))^H] \quad (28)$$

$$\boldsymbol{R} = \boldsymbol{S}\, E[\boldsymbol{x}(n)\boldsymbol{x}(n)^{\boldsymbol{H}}]\boldsymbol{S}^H + E[\boldsymbol{v}(n)\boldsymbol{v}(n)^{\boldsymbol{H}}] \quad (29)$$

$$\boldsymbol{R} = \boldsymbol{S}\boldsymbol{R}_{xx}\boldsymbol{S}^H + \sigma^2 \boldsymbol{I}_M \quad (30)$$

where E is the statistical expectation, $\sigma^2 \boldsymbol{I}_{\mathrm{M}}$ and $\boldsymbol{R}_{xx}$ denote the noise and the source correlation matrix, respectively. Moreover, we denote the eigenvectors of $\boldsymbol{R}$ as $\{\boldsymbol{e}_i, i = 1.....M\}$ and its eigenvalues as $\omega_1 \leq \omega_2 \leq \cdots \omega_{\mathrm{M}}$. Assuming $M \geq K$, the smallest $M - K$ eigenvalues of $\boldsymbol{R}$ correspond to the noise subspace. The eigen decomposition of $\boldsymbol{R}$ is represented as:

$$\boldsymbol{R} = \boldsymbol{E}_S \boldsymbol{\Lambda}_S \boldsymbol{E}_S^{\boldsymbol{H}} + \sigma^2 \boldsymbol{E}_N \boldsymbol{E}_N^{\boldsymbol{H}} \quad (31)$$

where $\boldsymbol{E}_S = [\boldsymbol{e}_1 .. \boldsymbol{e}_K] \in R^{M\,X\,K}$, $\boldsymbol{E}_N = [\boldsymbol{e}_{K+1} .. \boldsymbol{e}_M] \in R^{M\,X\,M-K}$ denote the signal and noise subspace and $\boldsymbol{\Lambda}_S$ represents the diagonal matrix containing the eigenvalues that correspond to the signal subspace.

In reality, however, the eigenvectors are not known a-priori and must be estimated from the received signal. We denote the estimated sample covariance matrix as:

$$\widehat{\boldsymbol{R}}_N = \frac{1}{N} \sum_{\boldsymbol{n}} \mathbf{y}(n)\mathbf{y}(n)^{\boldsymbol{T}} \quad (32)$$

and its associated eigenvectors as $\{\hat{\boldsymbol{e}}_i, i = 1.....M\}$ and eigenvalues as $\lambda_1 \leq \lambda_2 \leq \cdots \lambda_M$.

5.3 Subspace Based Methods

Array processing methods provide a robust signal processing tool to solve the inverse problem. Multiple Signal Classification (MUSIC) is a well-known subspace-based source localization algorithm that utilizes the eigen structure of the spatial covariance matrix and provides a computationally efficient alternative to maximum likelihood (ML) algorithms [2].

In cases where only a limited number of samples are available, the performance of the MUSIC algorithm degrades, since part of the energy from the noise subspace of the covariance matrix leaks into the signal subspace, causing the two subspaces to lose their orthogonality. In order to counter this problem, a new source localization technique called G-MUSIC is proposed in [4], which is a form of weighted MUSIC. Unlike MUSIC which only uses eigenvectors from the noise subspace, G-MUSIC uses all (signal and noise) eigenvectors of the data covariance matrix. The following sections provide details on the MUSIC and G-MUSIC algorithms.

5.3.1 MUSIC. From (27) it is clear that the received data vector $\boldsymbol{y}\,(n)$ is a linear combination of the columns of $\boldsymbol{S}$. Hence, the steering vectors span the signal subspace. The basic idea behind subspace identification algorithms, such as MUSIC, is based on the property that any vector present in the signal subspace is orthogonal to the noise subspace, i.e. $\boldsymbol{E}_N{}^{\mathrm{T}}\,\boldsymbol{s_k} = 0$.

Additionally, comparing (31) and (32) we find that the noise eigenvectors $\widehat{\boldsymbol{E}}_N$ of the sample covariance matrix are not exactly equal to $\boldsymbol{E}_N$; therefore $\widehat{\boldsymbol{E}}_N{}^{H}\,\boldsymbol{s_k}$ should have a small (but non-zero) norm. The MUSIC algorithm exploits this principle by searching for the deepest local minima of the cost function:

$$\eta_{MUSIC} = \boldsymbol{s_k^T}\,\widehat{\boldsymbol{E}}_N\,\widehat{\boldsymbol{E}}_N{}^{T}\,\boldsymbol{s}_k \tag{33}$$

Keeping the number of sensors (M) fixed and making appropriate statistical assumptions where the number of samples (N) increases without bound ($N\rightarrow\infty$), the MUSIC cost function is a good estimate of the deterministic original cost function. MUSIC is thus considered to be N- consistent; however the algorithm breaks down when the number of samples fall below a certain threshold, as shown in [4].

5.3.2 G-MUSIC. In order to localize sources when only finite sample support is available, a new weighted MUSIC estimator is proposed in [4] that is both M, N consistent. This method was recently used to estimate the direction of arrival (DOA) in radar applications.

The tools used to improve the asymptotic performance of MUSIC are based on G-estimation techniques that exploit results from random matrix theory. This method helps derive an M, N consistent estimator of the true covariance matrix for different

scalar functions. Such an estimator is referred to as G-MUSIC. The cost function is defined as [4]:

$$\eta_{G-MUSIC} = \boldsymbol{s}_k^T \left(\sum_{i=1}^{M} \varphi(i) \hat{e}_i \hat{e}_i^T \right) \boldsymbol{s}_k \tag{34}$$

where

$$\varphi(\mathrm{i}) = \begin{cases} 1 + \sum_{\mathrm{k=M-K+1}}^{\mathrm{M}} \frac{\lambda_\mathrm{k}}{\lambda_\mathrm{i}-\lambda_\mathrm{k}} - \frac{\mu_\mathrm{k}}{\lambda_\mathrm{i}-\mu_\mathrm{k}} & \mathrm{i} \leq \mathrm{M-K} \\ - \sum_{\mathrm{k=1}}^{\mathrm{M-k}} \frac{\lambda_\mathrm{k}}{\lambda_\mathrm{i}-\lambda_\mathrm{k}} - \frac{\mu_\mathrm{k}}{\lambda_\mathrm{i}-\mu_\mathrm{k}} & \mathrm{i} > \mathrm{M-K} \end{cases} \tag{35}$$

and $\mu_1 \leq \mu_2 \leq \cdots \ldots \leq \mu_M$ are the eigenvalues of $diag\,(\boldsymbol{\lambda}) - \frac{1}{N}\sqrt{\boldsymbol{\lambda}}\sqrt{\boldsymbol{\lambda}}^T$.

It can be seen from (34) and (35) that G-MUSIC uses all the eigenvectors of the covariance matrix, whereas MUSIC only uses the eigenvectors corresponding to the noise subspace. The signal subspace is included in the G-MUSIC estimator since low sample support causes the noise subspace to leak into the signal subspace, which in turn makes the two slightly non- orthogonal.

5.4 Calibration

In the case of brain source localization, the leadfield obtained as a solution to the forward problem is referred to as the *theoretical leadfield*. However, various anomalies can cause the measured leadfield to differ from the theoretical leadfield. These anomalies can arise due to e.g. co-registration and approximation of the head model with limited accuracy and discretization of the source space and are termed as calibration errors [5]. As such, array calibration is required to account for any discrepancies that may cause the actual leadfield to differ from the theoretical one [6].

In order to relate the modeled and measured leadfield, transfer function based calibration algorithms are now developed. These algorithms require prior knowledge about the geometry of the modeled array manifold and the leadfield of the guide sources.

Guide sources can be obtained by collecting strong focal evoked responses in the functionally mapped parts of the brain using applicable stimulation (auditory, somatosensory, visual, etc.). These accumulated evoked responses correspond to the *measured/actual leadfield* of the guide sources.

The perturbed measured leadfield is modeled as in [5]:

$$\boldsymbol{Z} = (\boldsymbol{A} + \Delta\boldsymbol{A})\boldsymbol{S} \tag{36}$$

where, $\boldsymbol{Z}$ and $\boldsymbol{S}$ are the measured and modeled leadfields, $\boldsymbol{A}$ and $\Delta\boldsymbol{A}$ are *M x M* matrices, the elements of which correspond to zero mean normal distributions.

5.4.1 External Calibration. Assuming that the locations of *L* guide sources *(L ≥ M)* are known, the modeled and measured leadfield are defined as follows:

$$\boldsymbol{S} \triangleq [s_1 \ldots\ldots s_L] \tag{37}$$

$$\boldsymbol{Z} \triangleq [z_1 \ldots\ldots z_L] \tag{38}$$

The calibration matrix $\boldsymbol{A} \in \mathrm{R}^{M \times M}$ is then computed such that, $\boldsymbol{Z} \approx \boldsymbol{AS}$, i.e. the modeled leadfield is a good approximation of the measured leadfield.

Two cost functions are defined in order to quantify the goodness of the approximation:

Least Squares Criterion: Define the cost function as*:*

$$\boldsymbol{J}_{LS} \triangleq \sum_{l=1}^{L} ||\boldsymbol{z}_l - \boldsymbol{A}\boldsymbol{s}_l||_F^2 \tag{39}$$

where, *F* denotes the Frobenius norm. Minimizing the above cost function yields:

$$argmin_A \boldsymbol{J}_{LS} = argmin_A ||\boldsymbol{Z} - \boldsymbol{AS}||_F^2 \tag{40}$$

Taking the derivative of the cost function with respect to $\boldsymbol{A}$ and equating it to zero yields:

$$\frac{\partial \boldsymbol{J}_{LS}}{\partial \boldsymbol{A}} = \frac{\partial}{\partial \boldsymbol{A}} tr\{(\boldsymbol{Z} - \boldsymbol{AS})^H x (\boldsymbol{Z} - \boldsymbol{AS})\}$$

$$= \mathbf{2}(\boldsymbol{Z} - \boldsymbol{AS})\boldsymbol{S}^H = \mathbf{0} \tag{41}$$

Thus, the optimum calibration matrix is:

$$\boldsymbol{A} = \boldsymbol{Z}\boldsymbol{S}^T(\boldsymbol{S}\boldsymbol{S}^T)^{-1} = \boldsymbol{Z}\boldsymbol{S}^{\#} \tag{42}$$

Beamsum Criterion: An alternative cost-function to least-squares is also presented.

Consider introducing an additional degree of freedom in (39) as:

$$\boldsymbol{J}_{BS} \triangleq \sum_{l=1}^{L} ||\boldsymbol{z}_l - \alpha_l \boldsymbol{A}\boldsymbol{s}_l||_F^2 \tag{43}$$

The analytical solution for α_l is found as follows:

$$\frac{\partial \boldsymbol{J}_{BS}}{\partial \alpha_l} = 2(\boldsymbol{AS})^H [\boldsymbol{Z} - \alpha_l \boldsymbol{AS}] = 2 (\boldsymbol{AS})^H \boldsymbol{Z} - 2\alpha_l [(\boldsymbol{AS})^H \boldsymbol{AS}] = 0 \tag{44}$$

Therefore, the optimum solution for $\alpha_l$is given by

$$\alpha_l = \frac{(\boldsymbol{AS})^H \boldsymbol{Z}}{||\boldsymbol{AS}||^2} \tag{45}$$

α_l can be viewed as the projection of the modeled leadfield onto the measured leadfield. The primary disadvantage of external calibration is that any changes in the environment will not be accounted for and will require the calibration to be repeated.

5.4.2 Auto Calibration. Contrary to external calibration, auto calibration only requires approximate information about the locations of the guide sources.

This technique employs a sequential optimization procedure to refine the estimates of the source locations and then update the calibration parameters according to changes in the environment. An initial estimate of the source locations is obtained provided that nominal knowledge of the calibration matrix is available.

We define $\overline{\boldsymbol{S}}$ as the modeled leadfield of *estimated* source locations and construct the calibration matrix. For least squares, the calibration matrix is computed as:

$$\overline{\boldsymbol{A}} = \mathbf{Z}\overline{\boldsymbol{S}} \tag{46}$$

The calibration matrix for beamsum is constructed by alternating between computing α_k from (45) and $\bar{A}$ as follows:

$$\overline{\boldsymbol{A}} = \boldsymbol{Z}\left(\overline{\boldsymbol{S}}\ \mathrm{diag}\left[\bar{\alpha}_1 \ldots \bar{\alpha}_l\right]\right)^{\#} \tag{47}$$

The initial guess for $\overline{\boldsymbol{A}}$ is provided by (46).

Fig.11 summarizes the iterative steps of the auto calibration algorithm.

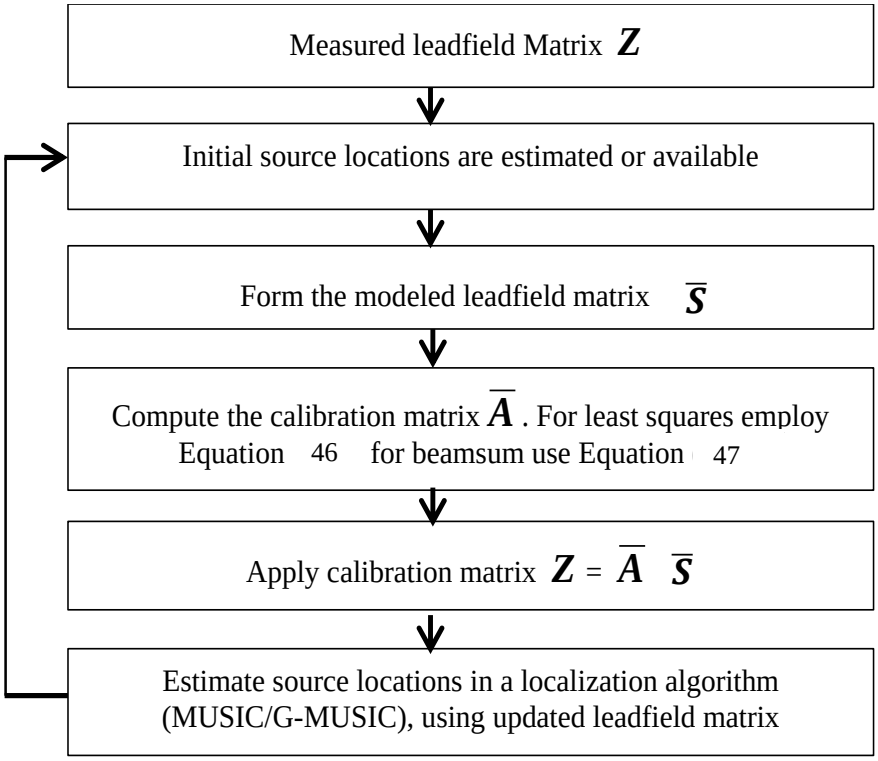

Figure 11: Flow diagram outlining the auto calibration process

We first obtain the measured leadfield matrix $\boldsymbol{Z}$ and the initial source estimates. The modeled leadfield matrix $\overline{\boldsymbol{S}}$ is obtained using the Brainstorm software. The calibration matrix $\overline{\boldsymbol{A}}$ is computed using either the beamsum or the least squares technique. The measured leadfield matrix is then updated via the calibration matrix. This updated measured leadfield is then applied to the localization algorithms MUSIC/G-MUSIC. This process is repeated until the system converges.

5.5 Simulation Setup: BRAINSTORM

As mentioned earlier in this thesis, an appropriate forward problem solution is required in order to accurately solve the inverse problem. Essentially, a volume head conductor model is assumed in order to produce mathematical models to represent the sources of brain activity. Using this model, and by introducing some constraining assumptions, the electric signals that appear outside the head can be estimated. These signals are then recorded by the sensors placed on the head.

The forward problem solution was obtained using the Brainstorm software. In this software, electrical activity recorded by sensors is produced by a set of electric dipoles at the cortex surface. The cortex surface has 15000 vertices with a dipole of

amplitude 1A.m placed at each vertex. The tessellated scalp is demonstrated in Fig.12. The orientation of the current dipoles in this work is assumed to be normal to the cortex surface, an assumption that is justified since the main contributors to the EEG signal are the pyramidal neurons that constitute 80% of the neocortical neurons [5].

The software computes the resulting electric field that the sensors would ideally record for each dipole and thus create a leadfield matrix of dimension M x N, where M is the number of sensors and N the number of sources (dipoles).

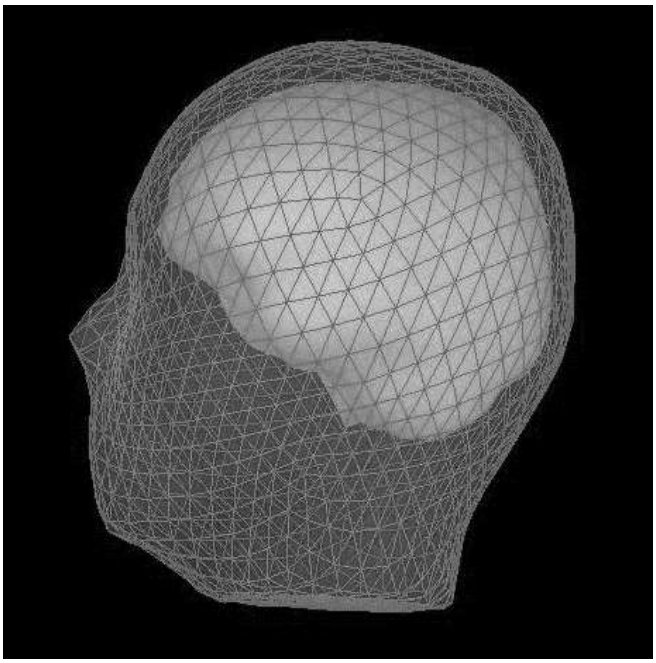

Figure 12: Tessellated scalp developed using Brainstorm

The head model computations have been done on the Colin27 head anatomy provided by the Montreal Neurological Institute which is an average of 21 T1-weighted scans of Colin Holmes brain, with resolution 1mm [15]. A three- shell spherical head model is used where the cortex, skull and scalp are represented by three concentric spheres with different diameters.

The main assumption made in this research is that each of the layers of the head model (cortex, skull and scalp) are considered to be isotropic and homogenous, which is not the case in reality. Therefore, in order to incorporate the inhomogeneity and anisotropy of the head model, one has to use advanced softwares that can produce boundary element method (BEM) or finite element method (FEM) based realistic head models.

Moreover, even generating simple head models such as spherical and BEM realistic head model (assuming homogeneity and isotropy) require that the absolute conductivity values of the head layers be specified in the software. The conductivity profile is usually quantified in terms of the conductivity ratio where the skull conductivity is the most important parameter in developing the head model. Various studies suggest different conductivity ratios. However the oldest and most often used ratio for brain: skull: scalp is 1:1/80:1. This ratio is also the default Brainstorm conductivity ratio and corresponds to absolute conductivity values of 0.33S/m: 0.0042 S/m: 0.33 S/m.

Next, synthetic EEG signals were produced for a BioSemi 64 electrode system (*M=64*). These sensors collect the electrical signals present outside the head, due to any neural activity in the brain, and usually come in standard cap form used in clinics to record brain signals from patients.

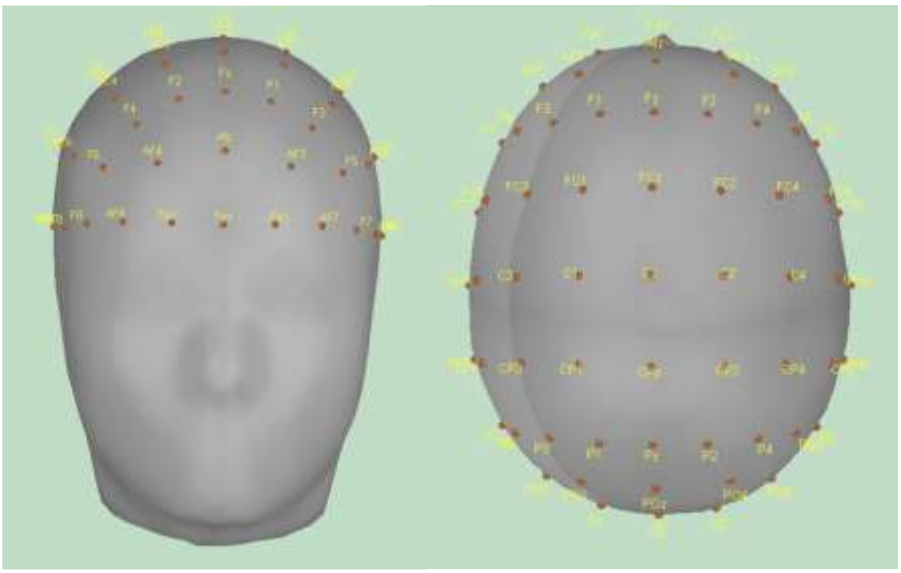

Figure 13: BioSemi 64 electrode system generated in Brainstorm

5.6 Results

We compare the performance of the G-MUSIC algorithm with the traditional MUSIC algorithm. Fig.14 indicates the localization of two sources placed at guide sources 600 and 603. It is clear that G-MUSIC has a more pronounced peak than MUSIC.

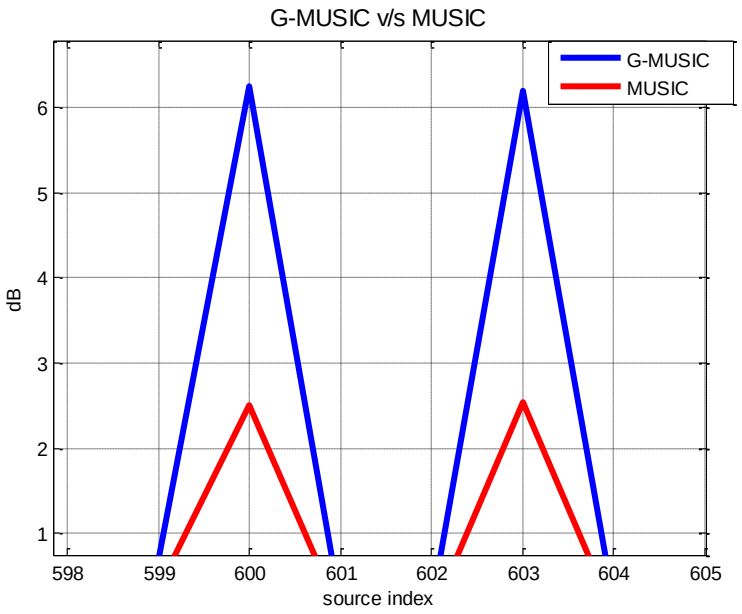

Figure 14: Localization of two sources placed at guide sources 600 and 603 using G-MUSIC and the MUSIC algorithm

Next, one of the four calibration techniques (least squares external and auto calibration as well as beamsum external and auto calibration) is used to account for any differences between the measured and modeled leadfield matrices. For calibration, 65 guide sources (calibration points) were selected from 3840 possible source locations ($1/12^{th}$ of the entire cortex surface).

Then, in order to verify the localization of 2 simulated random sources located at guide sources numbered 1710 and 2510 respectively (within the calibration region), the calibrated leadfield matrix is applied to either MUSIC or the G-MUSIC algorithm.

The effect of various calibration algorithms on the localization of sources was verified using G-MUSIC and MUSIC. Fig.15 compares the mean squared error (MSE) which is computed as the average of the squared error between the correct spectrum and acquired spectrum. This MSE is obtained by averaging over 30 realizations of the external and auto least squares calibration techniques for MUSIC and G-MUSIC.

It can be seen that external least squares calibration applied to G-MUSIC has lower MSE compared to the other techniques, as the number of samples decreases from 45 to 15.

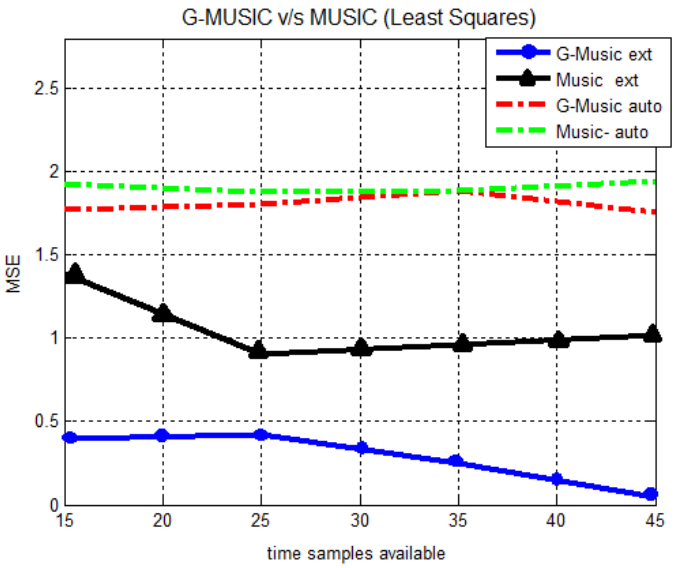

Figure 15: Comparative evaluation of the MSE achieved by MUSIC and G-MUSIC when least squares external and auto calibration techniques are applied

Similarly, Fig.16 represents the MSE in a scenario where external and auto beamsum calibration technique is applied to the traditional and weighted MUSIC algorithm.

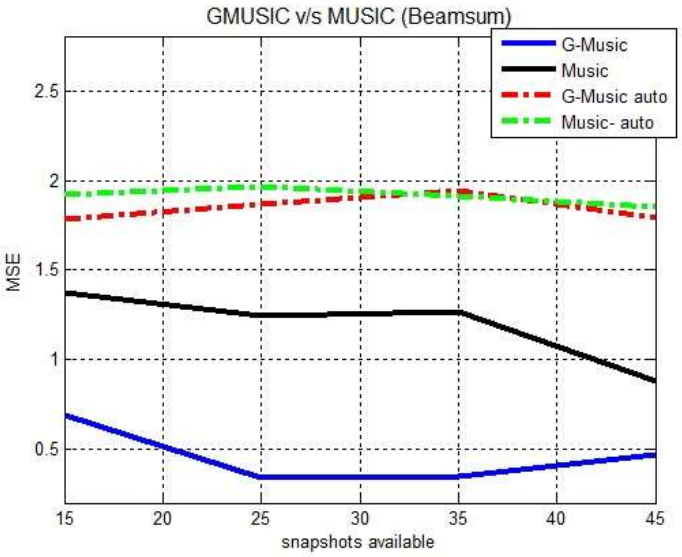

Figure 16: Comparative evaluation of the MSE achieved by MUSIC and G-MUSIC in the beamsum external and auto-calibration scenario

Fig.15 and Fig.16 indicate that when both the least squares and beamsum calibration techniques are applied to the MUSIC and G-MUSIC algorithm, external calibration technique when applied to the G-MUSIC algorithm provides lower MSE than all other techniques. Further, G-MUSIC when applied in conjunction with the auto

calibration technique, for both least squares and beamsum, provides lower MSE than MUSIC when used with the auto calibration technique

The rest of the figures represents the localization error where a threshold was applied in order to identify the strongest peaks as the recovered sources. The locations of the recovered test sources were compared to the ideal locations (in this case 1710 and 2510), whichever it happened to be closer to. The simulations were carried out for 30 time samples with increasing signal to noise ratio (SNR).

First, the various calibration algorithms are applied onto both the G-MUSIC and MUSIC algorithm. Observe that in Fig.17 when external calibration is used, G-MUSIC has a lower localization error (measured in cm) than MUSIC.

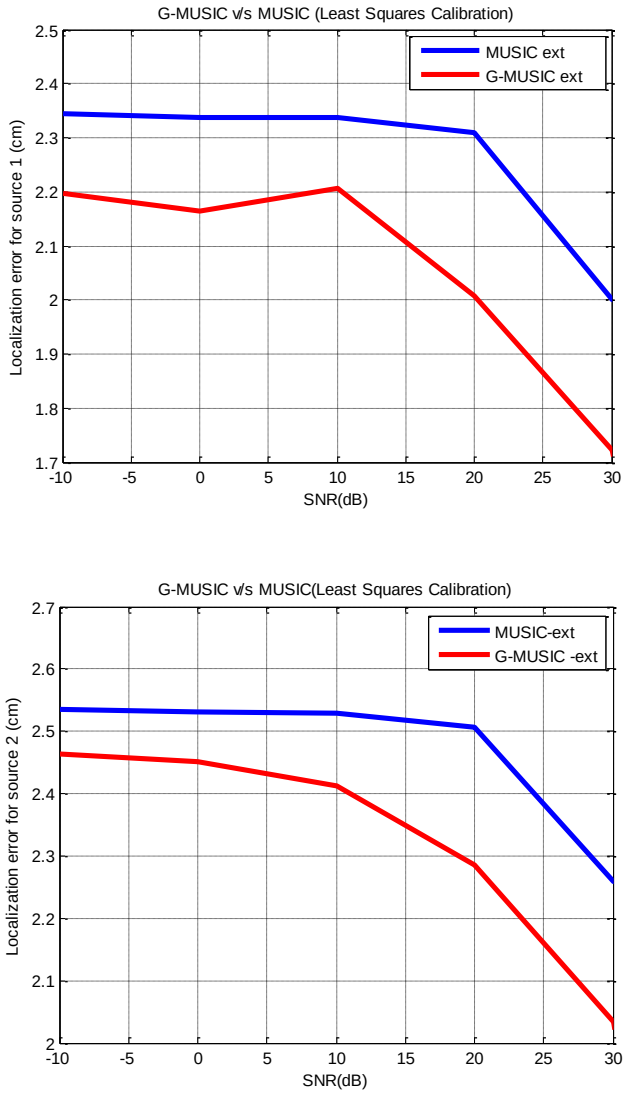

Figure 17: Least squares external calibration- comparative evaluation of the localization error achieved by MUSIC and G-MUSIC for source 1 and source 2

Similarly, Fig.18 suggests that G-MUSIC localizes sources with greater accuracy than MUSIC when least squares auto calibration is applied. At lower SNRs ranging from -10 to 10 dB the difference between the two calibrations is not very large. However as the SNR increases the difference between the two algorithms is quite prominent, where at an SNR of 40 for source 1, G-MUSIC with auto calibration has an error of about 1.5 cm whereas MUSIC when used with least squares based auto calibration has an error of about 2.8 cm.

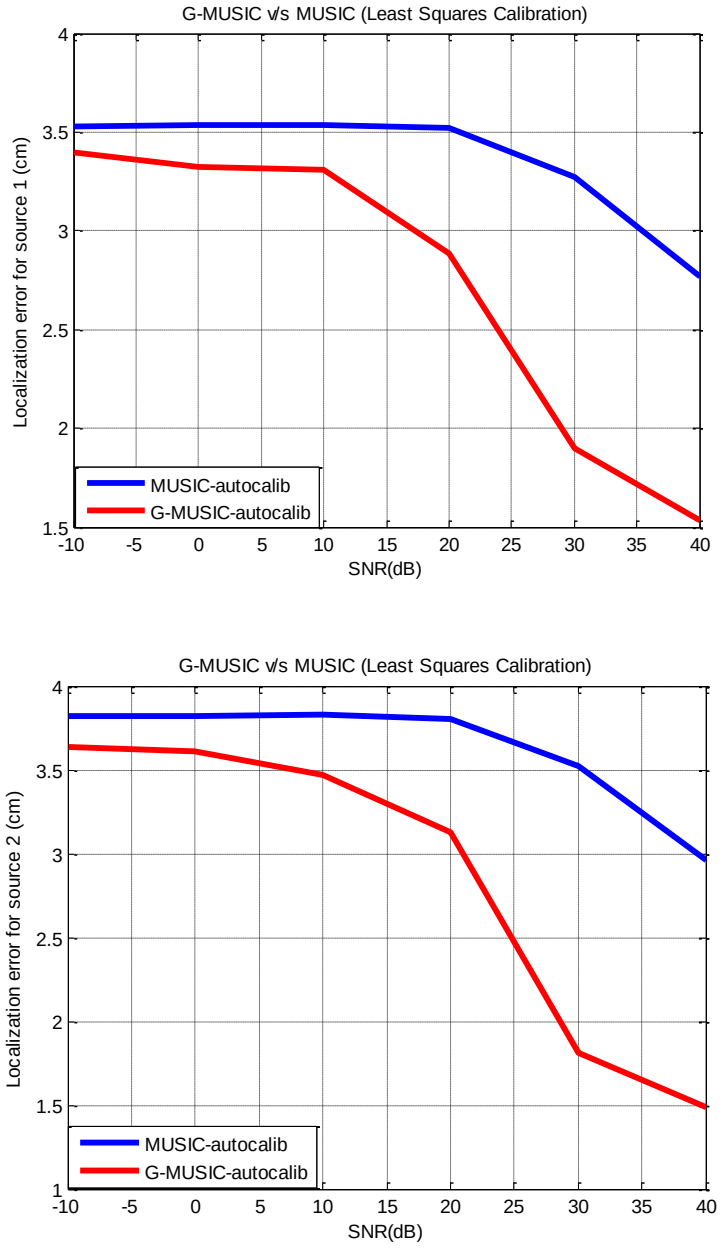

Figure 18: Least squares autocalibration-comparative evaluation of the localization error achieved by MUSIC and G-MUSIC for source 1 and source 2

Next, the external and auto calibration algorithms are compared to each other when used in conjunction with the G-MUSIC algorithm.Fig.19 shows that external least squares calibration provides lower localization error in the presence of large leadfield perturbation when compared to the auto calibration least squares method, at all SNR.

Since, beamsum calibrations produce similar results, the plots are not included.

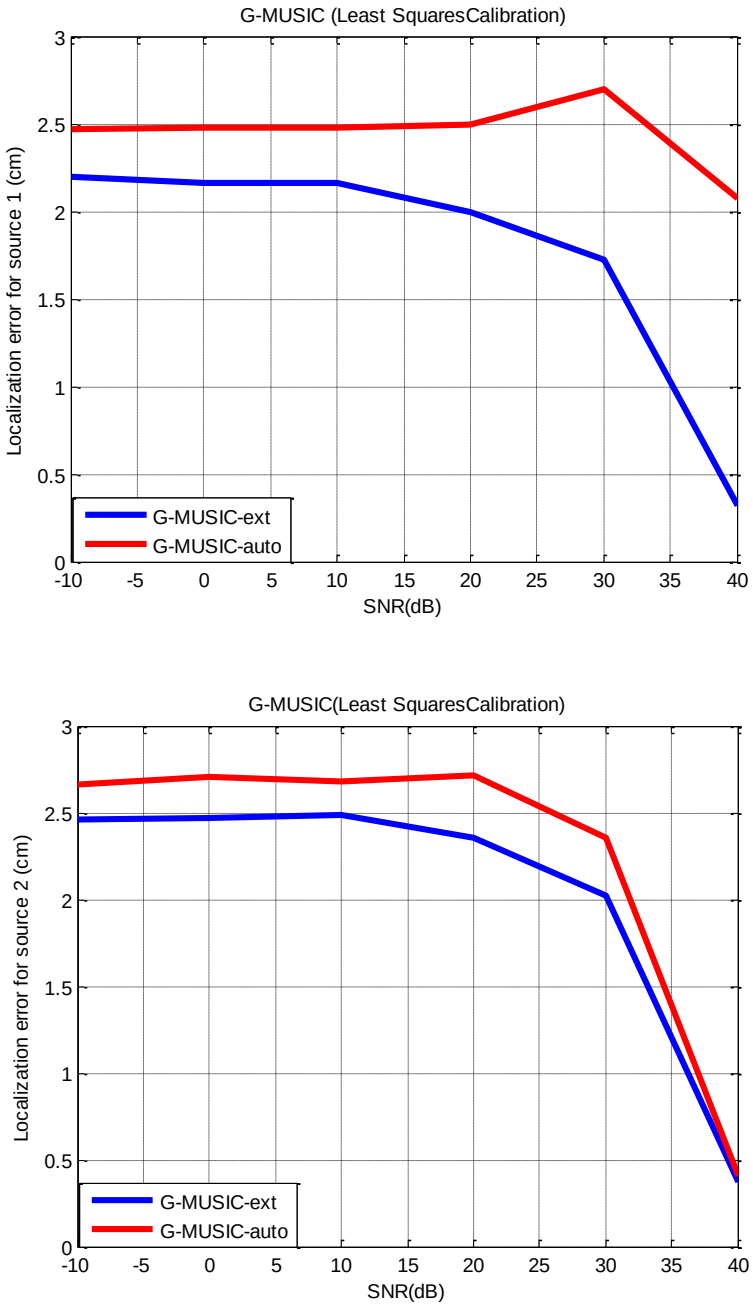

Figure 19: Comparative evaluation of the localization error achieved by least squares external and auto calibration for source 1 and source 2

Fig.20 compares least squares auto calibration to beamsum auto calibration. It can be seen that the localization error for beamsum is slightly lower than that of least squares for all SNR. This difference is prevalent especially at lower SNR for both sources, where at an SNR of 10 dB for source 1, least squares based G-MUSIC has an error of about 3.3 cm whereas G-MUSIC when applied using beamsum calibration has an error of about 3.1 cm. At higher SNR, the difference is almost negligible.

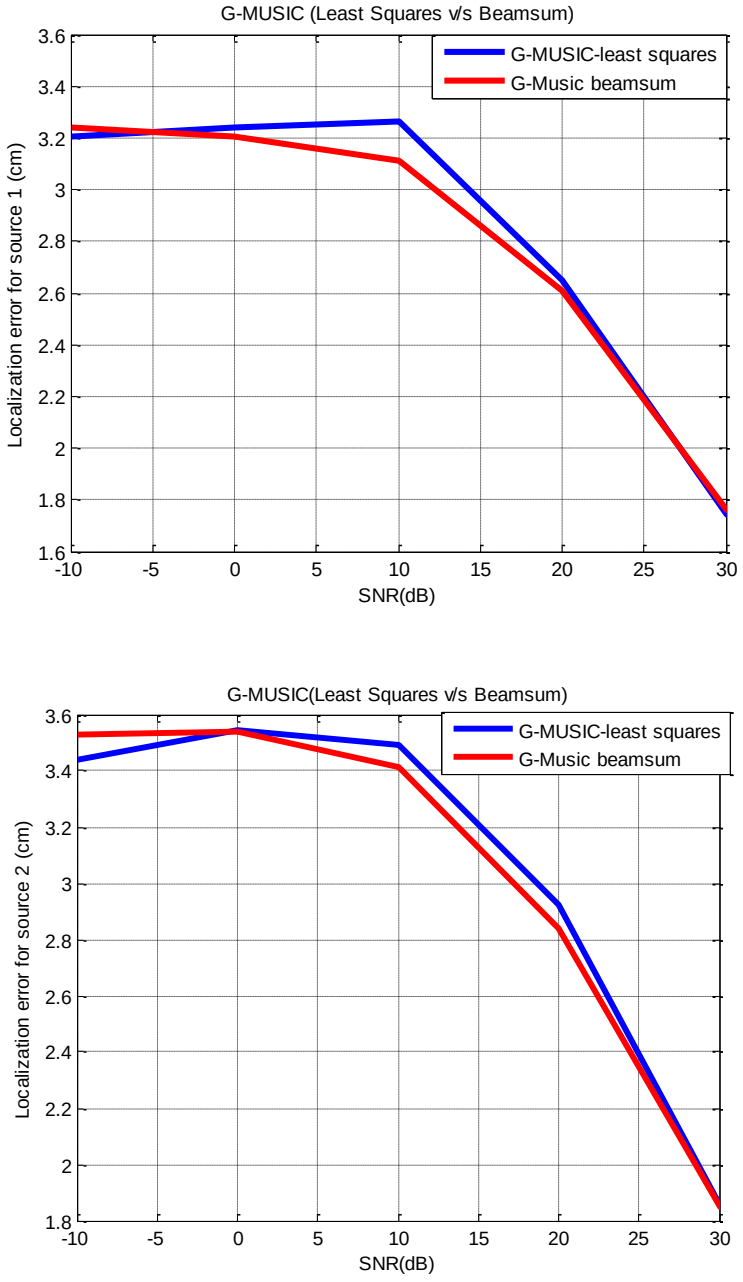

Figure 20: Auto calibration- comparative evaluation of the localization error achieved by least squares and beamsum autocalibration for source 1 and source 2

In all cases G-MUSIC outperforms MUSIC. Additionally, even though, in all cases, external calibration outperforms auto calibration. It should be noted that external calibration assumes precise apriori knowledge of the guide source locations, whereas auto calibration only requires a nominal location estimate. Thus, auto calibration provides a more practical solution while still maintaining a localization performance similar to that achieved with external calibration.

Chapter 6: Source Localization and Amplitude Estimation without Exact Knowledge of the Leadfield Matrix

As mentioned in Chapter 3, a precise volume conductor head model is essential in solving the inverse problem accurately. In order to realistically model the head, numerical algorithms such as boundary element method (BEM), finite element method (FEM) and finite difference method (FDM) must be implemented. These models incorporate the realistic geometry of the head by extracting surface boundaries for the skull, scalp and brain using magnetic resonance imaging (MRI) or computerized tomography (CT). Additionally, the head model also takes into account the electromagnetic properties of the volume that are mathematically expressed in the *leadfield* matrix. The leadfield matrix essentially comprises of vectors of amplitudes (steering vectors) received by the sensor array elements for each active source in the brain, and as mentioned earlier, is referred to as the forward problem solution. Although realistic head models improve localization accuracy, they are deemed impractical when incorporated as a part of an iterative solution due to the high computational complexity that accompanies creating the leadfield matrix. [28], [29] and [30] report that the time taken to build the leadfield matrix for a realistic head model extends up to several hours for an individual anatomy. Furthermore, employing a pre-determined realistic head model, or a simple single sphere head model, may not suffice due to various forward problem uncertainties, such as different conductivity profile or volume shape of an individual. These uncertainties are denoted as calibration errors. Therefore, array calibration is required to account for any discrepancies that may cause the actual leadfield matrix to deviate from the theoretical leadfield [6].

In the previous chapter we assumed that the leadfield matrix belonging to an individual head anatomy was perturbed due to various factors such as co-registration and approximation of the head model with limited accuracy etc., and were corrected using calibration algorithms. This chapter however, addresses the problem of localization without the exact knowledge of the leadfield matrix for an individual head anatomy, where the base leadfield matrix (theoretical) obtained using a realistic head model in Brainstorm, is used to acquire the actual leadfield matrix via the received EEG signal. An iterative algorithm is developed where the theoretical leadfield obtained using the Brainstorm software is applied to a high resolution localization algorithm to

obtain the initial source location estimates. On acquiring the initial locations and their corresponding steering vectors, a beamformer is designed in order to estimate the dipole source amplitudes. Furthermore, the received EEG signal is reconstructed using the estimated leadfield matrix and sources. A calibration matrix is then introduced to relate the reconstructed EEG signal to the actual EEG signal. This procedure is repeated until a convergence criteria is met. This procedure is summarized in Fig.21.

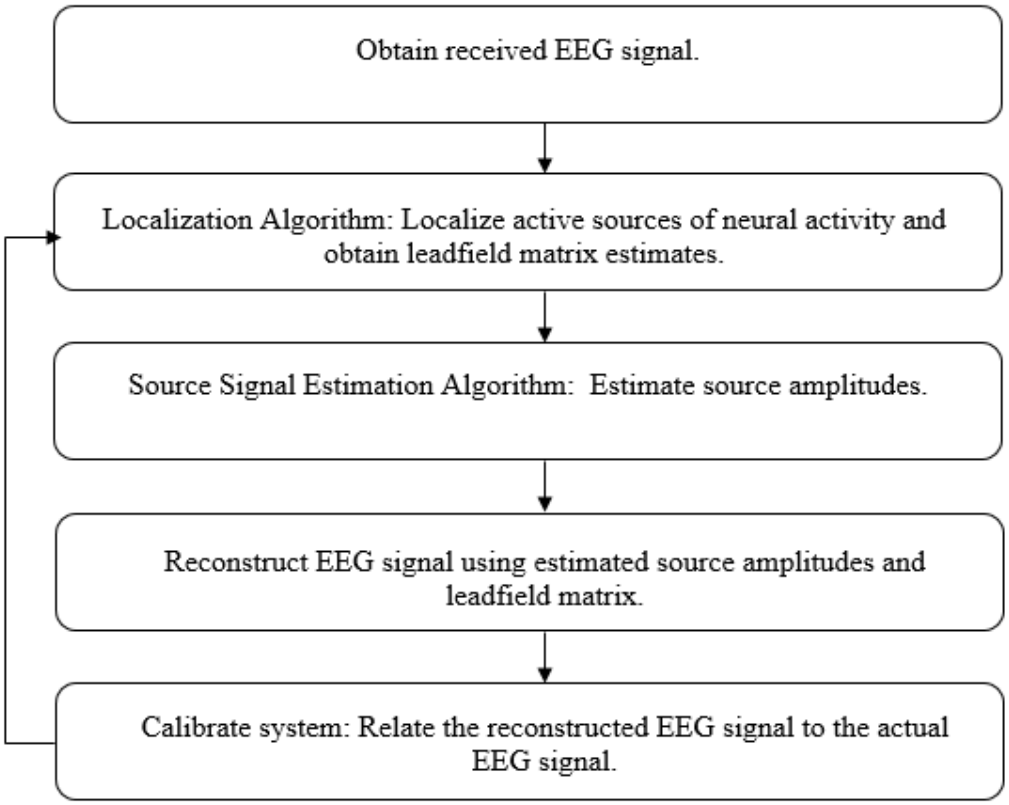

Figure 21 : Outline of proposed algorithm

6.1 Localization Algorithm: SAFFIRE

In Chapter 4, principles of phased array signal processing were introduced along with two direction of arrival (DOA) techniques, MUSIC and G-MUSIC. In this chapter another localization technique is introduced that has many advantages over other high resolution techniques mentioned in Chapter 4. G-MUSIC and MUSIC require the formation of the sample covariance matrix (SCM) from the available time samples. The disadvantages of SCM based localization techniques are as follows [31]:

(1) SCM based techniques require eigen decomposition increasing the computational complexity of the algorithm.

(2) When DOAs of the sources vary fast in time, the number of data samples decreases. This results in the construction of a less accurate SCM which thereby decreases the performance of the localization algorithm.
(3) The model order (number of sources of neural activity) must be estimated or known a-priori for most of the SCM based methods.

A high resolution DOA technique, that can tackle the above mentioned problems, is introduced in this chapter. Re-iterative super resolution (RISR) is a high resolution non-parametric algorithm based on the recursive implementation of the minimum mean squared error (MMSE) solution and has been used in radar applications. The main advantages of RISR essentially are:

(1) It operates on very low sample support.
(2) It does not require eigen decomposition and instead operates on non-coherent integration of many time samples
(3) It can automatically determine the number of sources present in the system.
(4) Furthermore, provided that the noise power is available, the noise information is included in the estimator.
(5) Similar to G-MUSIC it offers good robustness against temporal correlation.

The adaptation of RISR to neuroimaging applications is called the Source Affine Image Reconstruction algorithm (SAFFIRE).

6.1.1 SAFFIRE Algorithm. Similar to other functional neuroimaging techniques, SAFFIRE is predicated on the assumption that the measurements collected via an array of sensors can be modeled as the superposition of independent contribution from *K* sources distributed arbitrarily throughout the brain. Consider the received EEG signal measurement obtained from an array of *M* sensors for *N* time samples:

$$\boldsymbol{y}(n) = \boldsymbol{S}\boldsymbol{x}(n) + \boldsymbol{v}(n) \tag{48}$$

$\boldsymbol{x}(n)$ is a *K x 1* vector of source amplitudes, $\boldsymbol{S}$ is an *M x K* normalized leadfield matrix and $\boldsymbol{v}(n)$ is the zero mean additive Gaussian noise.

Essentially, SAFFIRE searches for an *M x K* adaptive filter bank $\boldsymbol{W}$ that minimizes the cost function

$$\boldsymbol{J} = E\left\{\left|\left|\boldsymbol{x}(n) - \hat{\boldsymbol{x}}(n)\right|\right|^2\right\} = E\left\{\left|\left|\boldsymbol{x}(n) - \boldsymbol{W}^T(n)\boldsymbol{y}(n)\right|\right|^2\right\} \tag{49}$$

where $(.)^T$ corresponds to the transposition and $E\{.\}$ represents the expectation. Further, $\hat{\boldsymbol{x}}(n)$ is the MMSE estimate of $\boldsymbol{x}(n)$.

Taking the derivative of $\boldsymbol{J}$ with respect to $\boldsymbol{W}$ and setting it to zero yields:

$$E\{2\,\boldsymbol{y}(n)[\,\boldsymbol{x}(n) - \boldsymbol{W}^T(n)\boldsymbol{y}(n)]\} = 0 \tag{50}$$

therefore,

$$\boldsymbol{W}(n)E\{\boldsymbol{y}(n)\boldsymbol{y}(n)^T\} = E\{\boldsymbol{y}(n)\boldsymbol{x}(n)^{\boldsymbol{T}}\} \tag{51}$$

As a result we obtain:

$$\boldsymbol{W}(n) = (E\{\boldsymbol{y}(n)\boldsymbol{y}(n)^{\boldsymbol{T}}\})^{-1}E\{\boldsymbol{y}(n)\boldsymbol{x}(n)^{\boldsymbol{T}}\} \tag{52}$$

Substituting (48) in (52) and assuming there is no correlation between the source amplitudes and noise, the filter bank is found to be [31]:

$$\boldsymbol{W}(n) = (\boldsymbol{S}E\{\boldsymbol{x}(n)\boldsymbol{x}(n)^T\}\boldsymbol{S}^T + E\{\boldsymbol{v}(n)\boldsymbol{v}(n)^T\})^{-1}\,\boldsymbol{S}E\{\boldsymbol{x}(n)\boldsymbol{x}(n)^T\} \tag{53}$$

Further simplification leads to,

$$\boldsymbol{W}(n) = (\boldsymbol{S}\boldsymbol{P}\boldsymbol{S}^T + \boldsymbol{R}_v)^{-1}\,\boldsymbol{S}\boldsymbol{P} \tag{54}$$

where, $\boldsymbol{R}_v$ is denoted as the noise correlation matrix and can be determined from the time samples where no evoked response is present.

On the contrary, the spatial power distribution $\boldsymbol{P}$ is not known a-priori and must be estimated using matched filter bank (MF) initializations [31]:

$$\hat{\boldsymbol{X}}_0 = \boldsymbol{S}^T\,\boldsymbol{Y} \tag{55}$$

$$\hat{\boldsymbol{P}}_0 = E\{\hat{\boldsymbol{x}}_{\boldsymbol{0}}(n)\hat{\boldsymbol{x}}_{\boldsymbol{0}}(n)^T\} \odot \boldsymbol{I}_{KxK} \tag{56}$$

where, $\odot$ is the Hadamard product and $\boldsymbol{I}$ corresponds to the identity matrix and enforces that the sources are temporally uncorrelated.

Additionally, this algorithm operates on each time sample individually or combines the power estimates through non coherent integration, thereby solving the issue of temporal correlation. Nonetheless, having coherent sources is similar to reduction in sample support (time samples) and thus may degrade the performance of the algorithm to some extent [32].

6.1.2 Non coherent Integration. In order to provide greater robustness to noise for *N* time samples of measurements, non-coherent integration of the SAFFIRE algorithm is implemented where the received signal is denoted as:

$$\boldsymbol{Y} = [\boldsymbol{y}(n)\ \ \boldsymbol{y}(n+1) \dots \dots \boldsymbol{y}(n+N-1)] \tag{57}$$

As in section 6.1.1, the aggregate filter bank, in order to determine *N* source amplitudes, is found to be:

$$\overline{\boldsymbol{W}} = (\boldsymbol{S}\overline{\boldsymbol{P}}\boldsymbol{S}^T + \boldsymbol{R}_v)^{-1}\,\boldsymbol{S}\overline{\boldsymbol{P}} \tag{58}$$

where, the initializations are done as follows:

$$\widehat{\boldsymbol{X}}_0 = \boldsymbol{S}^T\,\boldsymbol{Y} \tag{59}$$

$$\overline{\boldsymbol{P}}_0 = \frac{1}{N}\sum_{\tau=0}^{N-1} \widehat{\boldsymbol{x}}_0(n+\tau)\,\widehat{\boldsymbol{x}}_0(n+\tau)^T \odot \boldsymbol{I}_{KxK} \tag{60}$$

The source amplitudes and average spatial power distribution for *N* time samples are then estimated:

$$\widehat{\boldsymbol{X}} = \overline{\boldsymbol{W}}^T\,\boldsymbol{Y} \tag{61}$$

$$\overline{\boldsymbol{P}} = \frac{1}{N}\sum_{\tau=0}^{N-1} \widehat{\boldsymbol{x}}(n+\tau)\ \ \widehat{\boldsymbol{x}}(n+\tau)^T \odot \boldsymbol{I}_{KxK} \tag{62}$$

where, $\widehat{\boldsymbol{X}} = [\widehat{\boldsymbol{x}}(n)\ \ \widehat{\boldsymbol{x}}(n+1) \dots \dots \widehat{\boldsymbol{x}}(n+N-1)]$ is an *K x N* matrix comprised of source amplitude estimates for *N* time samples.

Equations (58), (61) and (62) encompass the iterative steps of the SAFFIRE algorithm. As reported in [31], the algorithm converges in maximum of 15 iterations. The diagonal elements of the matrix $\sqrt{\overline{\boldsymbol{P}}}$ correspond to the spectrum and provide an estimate of the average amplitude distribution.

6.1.3 Affine Transform of Solution Space. Sources present on the surface of the cortex are closer to the EEG sensors and therefore their steering vectors have larger norms than sources that are located deeper in the cortex. This causes a bias to occur for the superficial sources in some localization algorithms, such as the minimum norm estimate (MNE), as a result of which various weighted minimum norm techniques are proposed to account for the bias [33]. The SAFFIRE algorithm on the other hand is altered in order to provide all sources with an equal opportunity in the localization process; this is achieved by normalizing all columns of the leadfield matrix $\boldsymbol{S}$.

The main advantage of this recursive algorithm, for the purpose of brain source localization, is its ability to determine the model order (number of sources), their locations and the source amplitudes. However, these source amplitudes can be approximated only for slight modeling errors using an iterative calibration term [5], [31]. When a large perturbation is present in the actual leadfield matrix, the SAFFIRE algorithm is unable to recover the source amplitudes accurately. Therefore, an alternative signal estimation technique must be used in order to recover the source amplitudes with a better accuracy.

6.2 Signal Estimation Algorithm: Minimum Variance Beamformer (MVB)

In order to account for greater perturbations in the leadfield matrix, the MVB is implemented in this chapter for the estimation of source amplitudes. The power of the received signal in all possible directions is measured by the beamformer. Mathematically, the problem is expressed as [34]:

$$minimize \ \ \boldsymbol{h}^{\boldsymbol{T}} \boldsymbol{R}_{\boldsymbol{y}} \boldsymbol{h}$$

$$subject\ to\ \boldsymbol{h}^{\boldsymbol{T}} \boldsymbol{S} = \mathbf{1} \tag{63}$$

where $\boldsymbol{h}$ is the weight vector and $\boldsymbol{R}_{\boldsymbol{y}}$ is the covariance of the received signal.

Furthermore, the constraint guarantees that the signal passes through the beamformer undistorted. The minimum variance beamformer requires only the steering vector related to the desired signal. The analytical solution to (63) using Lagrange multiplier is given by [34]:

$$\boldsymbol{h}_k = \frac{\boldsymbol{R_y}^{-1}\boldsymbol{s}_k}{\boldsymbol{s}_k^T\,\boldsymbol{R_y}^{-1}\,\boldsymbol{s}_k} \tag{64}$$

In order to address the uncertainties in the leadfield matrix a regularization method, denoted as diagonal loading, is implemented. The weights of the regularized beamformer has a solution [34]:

$$\boldsymbol{h}_k = \frac{(\boldsymbol{R_y}+\mu\boldsymbol{I})^{-1}\boldsymbol{s}_k}{\boldsymbol{s}_k^T\,(\boldsymbol{R_y}+\mu\boldsymbol{I})^{-1}\,\boldsymbol{s}_k} \tag{65}$$

where $\mu > 0$. The source amplitudes are then estimated using:

$$\hat{\boldsymbol{x}}_k = \boldsymbol{h}_k^{\boldsymbol{T}}\,\boldsymbol{Y} \tag{66}$$

As a result, the signal of interest can be extracted while suppressing any interference and noise.

6.3 Calibration

In order to obtain a close estimate of the source location and amplitudes, we apply a calibration matrix to relate the actual received EEG signal $\boldsymbol{Y}$ and the estimated EEG signal $\widehat{\boldsymbol{Y}}$, reconstructed using estimates of the steering vectors (SAFFIRE algorithm) and source amplitudes (beamformer) $\widehat{\boldsymbol{Y}}$. The calibration matrix $\widehat{\boldsymbol{A}} \in \mathrm{R}^{M\,\mathrm{x}\,M}$ is then computed such that, $\boldsymbol{Y} \approx \widehat{\boldsymbol{A}}\,\widehat{\boldsymbol{Y}}$.

Define a cost function in order to obtain a solution for $\widehat{\boldsymbol{A}}$ as*:*

$$\boldsymbol{J}_{BS} \triangleq \sum_{l=1}^{K} ||\boldsymbol{y}_n - \alpha_n \widehat{\boldsymbol{A}}\,\hat{\boldsymbol{y}}_n||_F^2 \tag{67}$$

where *F* denotes the Frobenius norm and α_n can be viewed as the projection of the estimated EEG signal onto the actual EEG signal . The optimum solution for α_n is given by

$$\alpha_n = \frac{(\boldsymbol{A}\hat{\boldsymbol{y}}_n)^H \boldsymbol{y}_n}{\left||\boldsymbol{A}\hat{\boldsymbol{y}}_n|\right|^2} \tag{68}$$

Minimizing the cost function in (67) yields:

$$argmin_{\hat{A}}\,\boldsymbol{J}_{BS} = argmin_{\hat{A}}\,||\boldsymbol{Y} - \alpha\widehat{\boldsymbol{A}}\,\widehat{\boldsymbol{Y}}||_F^2 \tag{69}$$

Taking the derivative of the cost function with respect to $\widehat{\boldsymbol{A}}$ and equating it to zero yields:

$$\frac{\partial \boldsymbol{J_{BS}}}{\partial \widehat{\boldsymbol{A}}} = \frac{\partial}{\partial \widehat{\boldsymbol{A}}}\, tr\left\{ \left(|\boldsymbol{Y} - \alpha \widehat{\boldsymbol{A}}\, \widehat{\boldsymbol{Y}}\right)^{H} x \left(|\boldsymbol{Y} - \alpha \widehat{\boldsymbol{A}}\, \widehat{\boldsymbol{Y}}\right)\right\}$$

$$= \mathbf{2}\left(|\boldsymbol{Y} - \alpha \widehat{\boldsymbol{A}}\, \widehat{\boldsymbol{Y}}\right)|\alpha \widehat{\boldsymbol{Y}}^{H} = \mathbf{0} \qquad (70)$$

Thus, the optimum calibration matrix is:

$$\widehat{\boldsymbol{A}} = \boldsymbol{Y}(\widehat{\boldsymbol{Y}}\text{diag}\left[\bar{\alpha}_1 \ldots \bar{\alpha}_n\right])^{\#} \qquad (71)$$

It is important to note, that as long as the error associated with the initial guess regarding the location and the amplitude of the sources is relatively small, the iterative algorithm will provide a good solution. Fig.22 outlines the proposed algorithm.

Algorithm: Localization without exact knowledge of the leadfield matrix

Initializations:

i) Given received EEG signal $\boldsymbol{Y}$ for N time samples
ii) Obtain theoretical leadfield matrix $\boldsymbol{S}$
iii) Initialize calibration matrix $\widehat{\boldsymbol{A}}^{\boldsymbol{0}} = \boldsymbol{I}$, $\boldsymbol{S}^{\boldsymbol{0}} = \widehat{\boldsymbol{A}}^{\boldsymbol{0}}\boldsymbol{S}$, $i = 0$

while localization error > threshold **do**

1. **Localization:** Obtain the "SAFFIRE spectrum" using $\bar{\boldsymbol{x}} = diag\sqrt{\bar{\boldsymbol{P}}}$. Determine the number of sources, their locations and corresponding steering vectors $\widehat{\boldsymbol{s_k}}$ via the peaks in $\bar{\boldsymbol{x}}$.

2. **Signal Estimation:** Estimate weight vectors and their corresponding source amplitudes $\widehat{\boldsymbol{x_k}} = \boldsymbol{h_k}^{\boldsymbol{T}}\boldsymbol{Y}$

3. Reconstruct estimated received EEG signal $\widehat{\boldsymbol{Y}}^{\boldsymbol{i}} = \widehat{\boldsymbol{A}}^{\boldsymbol{i}}\left(\widehat{\boldsymbol{S}}\widehat{\boldsymbol{X}}\right)$

4. Estimate ${\alpha_n}^i$ using (68)

5. **Calibration:** Update calibration matrix $\widehat{\boldsymbol{A}}^{\boldsymbol{i+1}} = \boldsymbol{Y}(\widehat{\boldsymbol{Y}}^{\boldsymbol{i}}\text{diag}\left[\bar{\alpha}_1 \ldots \bar{\alpha}_n\right])^{\#}$

6. Update $\boldsymbol{S}^{\boldsymbol{i+1}} = \widehat{\boldsymbol{A}}^{\boldsymbol{i+1}}\,\boldsymbol{S}^{\boldsymbol{i}}$

7. *i=i+1*

8. Calculate localization error

end while

Figure 22: Proposed algorithm procedure

6.4 Simulated Data

6.4.1 Simulation setup. The forward problem solution in this thesis was obtained using the Brainstorm software. A boundary element method (BEM) head model is used and the head model computations have been done on a realistic head anatomy with a resolution of 4 mm, which is a magnetic resonance imaging (MRI) volume provided by the French public research institute INRIA [15].

Next, synthetic EEG signals were produced for a BioSemi 64 electrode system (*M=64*). The modeled leadfield is obtained from Brainstorm and the perturbed measured leadfield is modeled as in [35]:

$$\boldsymbol{Z} = (\boldsymbol{A} + \Delta\boldsymbol{A})\boldsymbol{S} \tag{72}$$

where $\boldsymbol{A}$ and $\Delta\boldsymbol{A}$ are *M x M* matrices, the elements of which correspond to zero mean normal distributions.

The algorithm was applied to the region of interest comprising of 1280 vertices on the brain, where synthetic EEG signal consisting of 2 sources were simulated with 15% perturbation and 50 time samples with an SNR of 30 dB.

Initially, the SAFFIRE algorithm was applied in order to locate the sources with the largest peaks. The corresponding steering vectors (columns of the leadfield matrix) were then obtained and applied to the beamformer algorithm in order to estimate the source amplitudes. Finally, the estimated EEG signal was reconstructed and compared to the actual received signal via a calibration matrix. This procedure was repeated until a certain convergence criteria was met.

6.4.2 Results. Fig.23 shows the recovered sources mapped on the cortex before and after the algorithm is applied. Furthermore, Table 1 represents the localization error before and after calibration, where a threshold was applied in order to identify the strongest peaks as the recovered sources.

The locations of the recovered test sources were compared to the ideal locations (in this case 165 and 285) at each iteration. In this simulation setup, the algorithm stops when the localization error falls below a certain threshold.

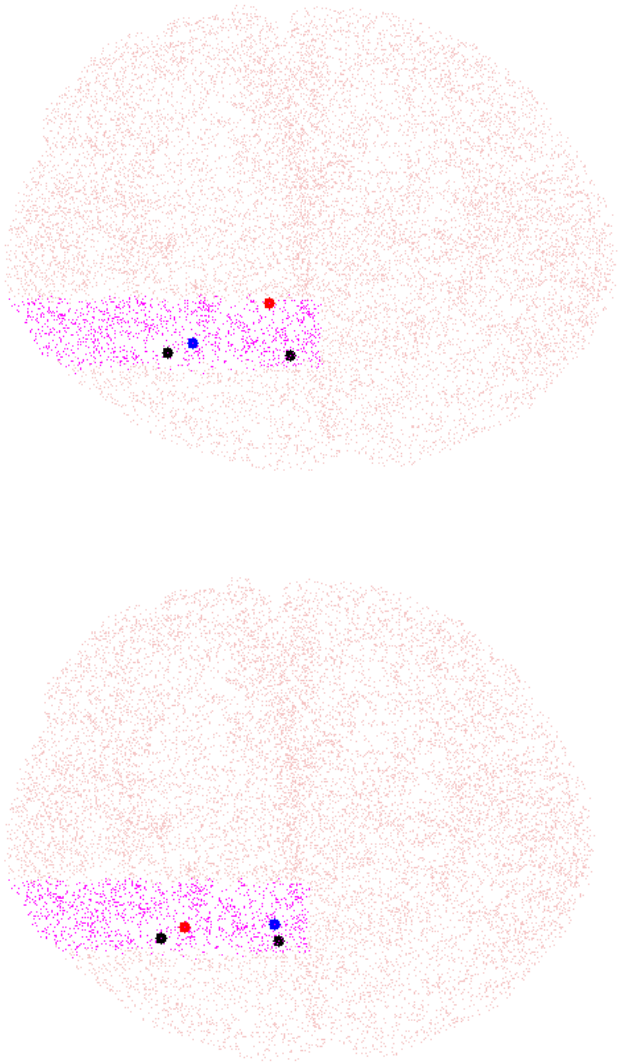

(b)

Figure 23: Recovered sources mapped on the cortex (a) before (b) after applying the proposed algorithm

The red point corresponds to the recovered source with the strongest spatial power whereas the blue point refers to the weaker source. The black points refers to the ideal locations (in this case 165 and 285).

Table 1: Localization Error before and after calibration

	Before Calibration	After Calibration
Localization Error : Point 1 (cm)	3.0133	2.6244
Localization Error : Point 2 (cm)	3.0628	0.7143

Fig.24 (a) and Fig.24 (b) illustrate the SAFFIRE spectrum obtained before calibration and after calibration. Within a few iterations, the algorithm recognizes two strong sources similar to the true spectrum shown in Fig.24 (c) where the source locations are denoted by the x axis.

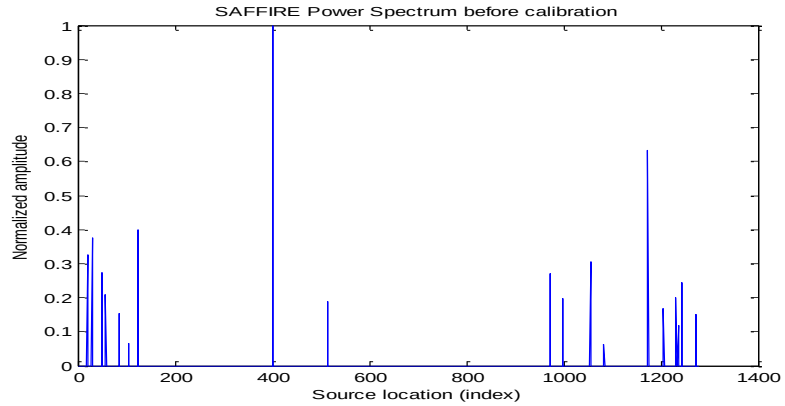

(a)

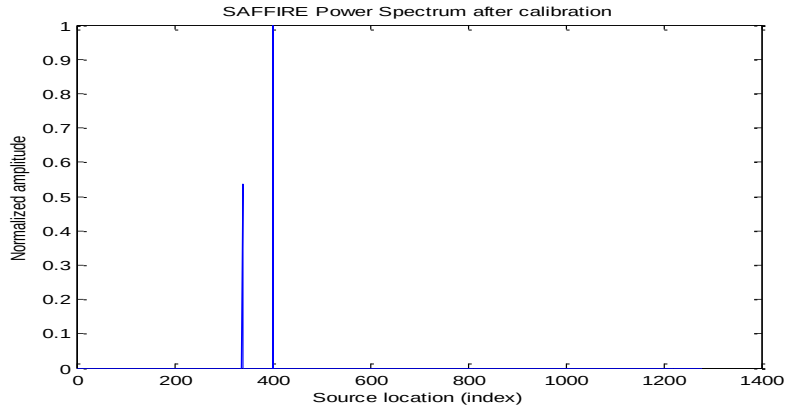

(b)

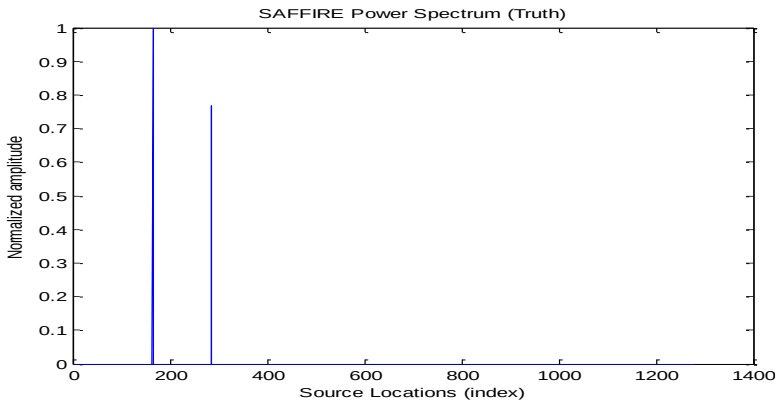

(c)

Figure 24: SAFFIRE power spectrum (a) before calibration (b) after calibration (c) truth

Fig.25 (a) indicates that before the calibration algorithm is applied, the recovered signal is not a very good estimate of the original signal. However, Fig.25 (b) shows that after the proposed algorithm is applied, within a few iterations, the estimated source 1 amplitude is recovered.

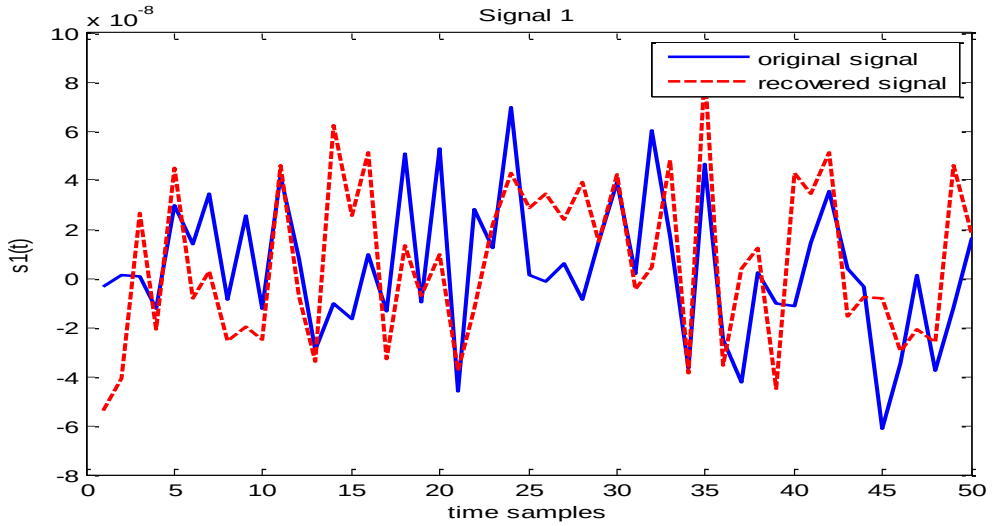

(a)

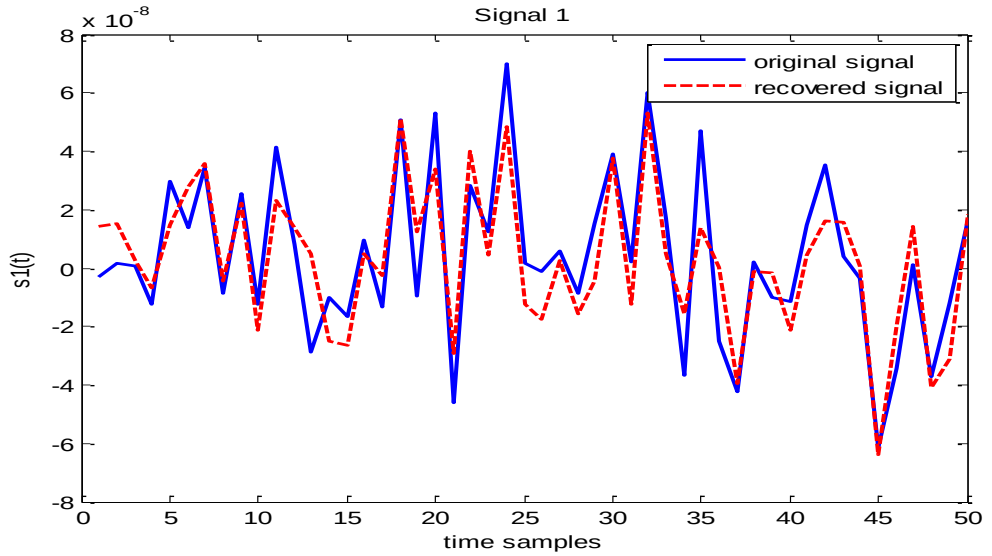

(b)

Figure 25: Source 1 amplitude estimate (a) before (b) after calibration

Similarly, an approximate estimate of source 2, after a few iterations, is recovered in Fig.26, where the same trend as Fig.25 is observed before and after the calibration algorithm converges.

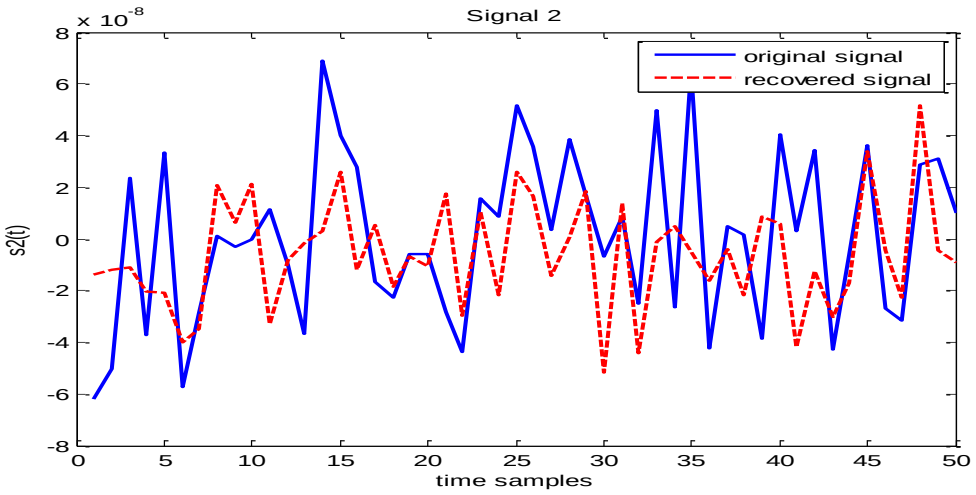

(a)

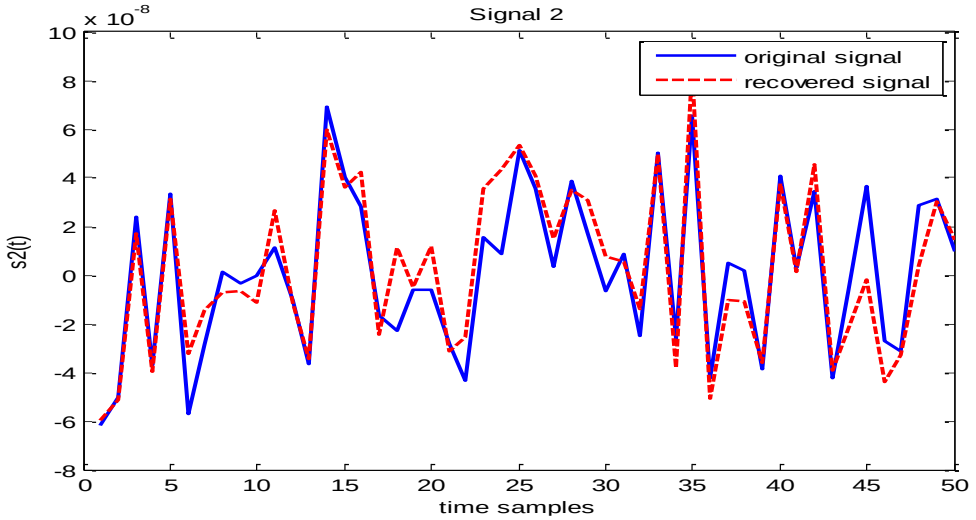

(b)

Figure 26: Source 2 amplitude estimate (a) before (b) after calibration

The average localization error, in centimeters, is described in Fig.27. The localization error was found by averaging over 300 iterations of the algorithm for each SNR with a 15 percent perturbation in the leadfield matrix. The localization error falls to about 1.8963 cm for source 1 and 1.5051 cm for source 2, as the SNR reaches 30 dB when the proposed algorithm is applied. The algorithm is compared to the least squares solution. For the least squares solution, the source amplitude is recovered as follows:

$$\hat{\boldsymbol{x}} = \boldsymbol{Y}\,(\widehat{\boldsymbol{A}}\widehat{\boldsymbol{S}})^{\#} \tag{73}$$

The proposed algorithm provides a localization error of 2.3973 cm for -20 dB whereas the least squares solution yields a localization error of 2.4598 cm for source 1.

Similarly, for source 2, the proposed algorithm provides a localization error of 2.2974 cm which is lower than the localization error given by the least squares solution, which for this source is 2.6956 cm.

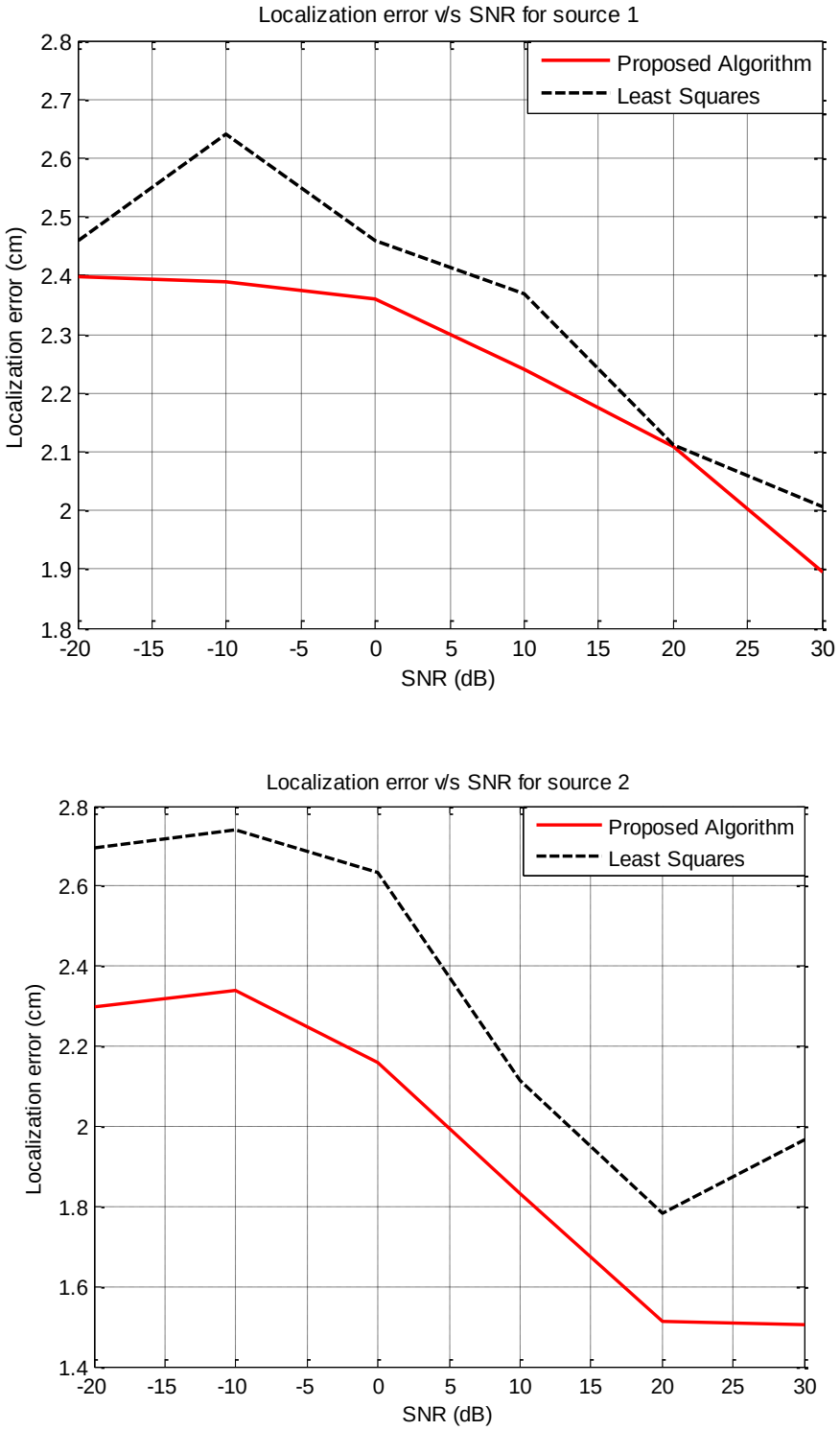

Figure 27: Average localization error (cm) for source 1 and 2 v/s SNR (dB)

Moreover, it was observed that the algorithm generally converges after 20 iterations which takes around 16.279746 seconds of computational time where each iteration takes approximately 0.825524 seconds.

Therefore, the above results indicate that even when exact knowledge of the leadfield matrix is not available, a good estimate of the source location and its amplitude can be obtained when the proposed algorithm is applied to simulated EEG signal received at the sensors. However, in order to guarantee a good performance, the error associated with the initial guess regarding the location and the amplitude of the sources must be relatively small.

Chapter 7: Experimental Data

7.1 Experimental Setup

The EEG/ERP system consists of the EEG cap, 64-channel EEG amplifier, data acquisition system and the ASA Lab software for checking the electrode impedance, acquiring, displaying and storing EEG signal (ANT B.V., Enschede, Netherlands). Furthermore, the data is collected under a controlled environment where the electrode placement follows the 10-20 system. Moreover, the EEG is filtered between 0.1-60 Hz and sampled at 256 samples per second. Next, the ERP signal is extracted, which requires ensemble averaging. To achieve this, a controller PC is used, which displays the target and non-target images on the screen. The target images in this experiment correspond to human faces, whereas any other image is regarded as non-target. The controller PC, also generates through a MATLAB code, an event marker signal that is applied to the EEG amplifier just before the image is shown on the screen. The event marker signal is later used to segment the EEG and extract the signal frames corresponding to the target and non-target images. Ensemble averaging is then performed to produce one average matrix for the target image and one for the non-target images. Further signal processing is done on the raw EEG data matrices to extract the P300-ERP from a single stimulus.This experimental study protocol was approved by the Institutional Review Board at the National University of Singapore.

The P300 EEG signal for a single subject is utilized in the algorithm described in Chapter 6. Since, the EEG signal was collected when a target image was shown to the subject, it is expected that the sources in the Fusiform Face Area (FFA) will be activated. Functional magnetic resonance imaging (fMRI) studies have indicated that FFA responds more strongly to human faces than any other kind of object [36]. FFA is located in the fusiform gyrus (medial occipitotemporal cortex) and specializes in face recognition and trial-by- trial face identification and detection tasks [37].

7.2 Results

A threshold is applied to the SAFFIRE spectrum in order to determine the strong peaks corresponding to the strongest sources. The iterations are halted when the localization error between two consecutive iterations is negligible. Initially a specific region of interest is picked on the left cortex, where the two active sources are plotted.

Two strong sources are recovered when the algorithm is applied to the experimental data and are plotted on a 3-d cortex in Fig.28.

Furthermore, Fig.29 illustrates the SAFFIRE spectrum obtained before and after calibration. It is clear that after applying the algorithm within a few iterations, two strong sources are detected. The strongest source with an amplitude of 1 is plotted in red on the 3-d cortex, whereas the relatively weaker source of an amplitude 0.593 is plotted in blue.

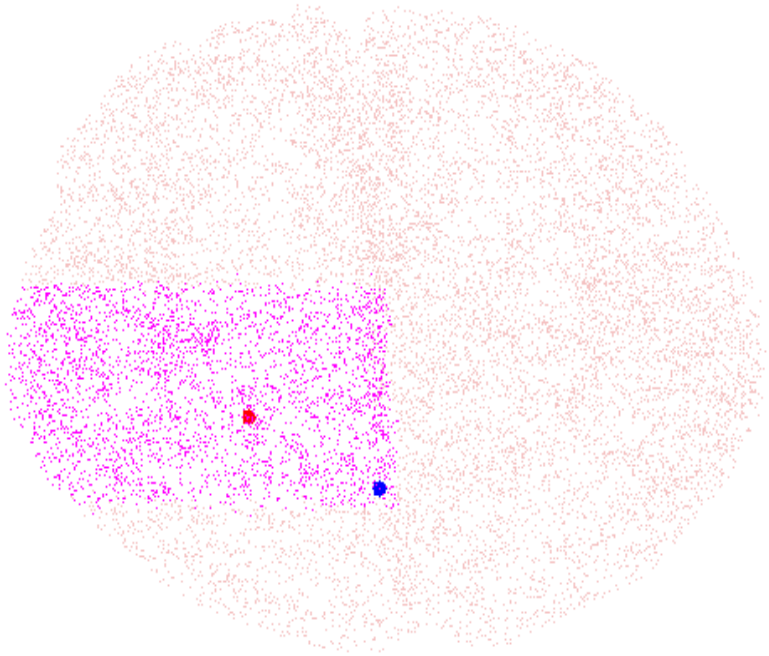

Figure 28: Recovered sources mapped on the cortex after applying the proposed algorithm

In Fig.29 (a) the SAFFIRE spectrum indicates that there are various active sources present on the cortex, before the calibration algorithm is applied. However, once a threshold is applied to the SAFFIRE algorithm, two strong sources are visible in the SAFFIRE spectrum illustrated in Fig. 29 (b).

The steering vectors (columns) of the location of the strong peaks are then obtained and applied to the beamformer algorithm in order to determine the respective amplitudes.

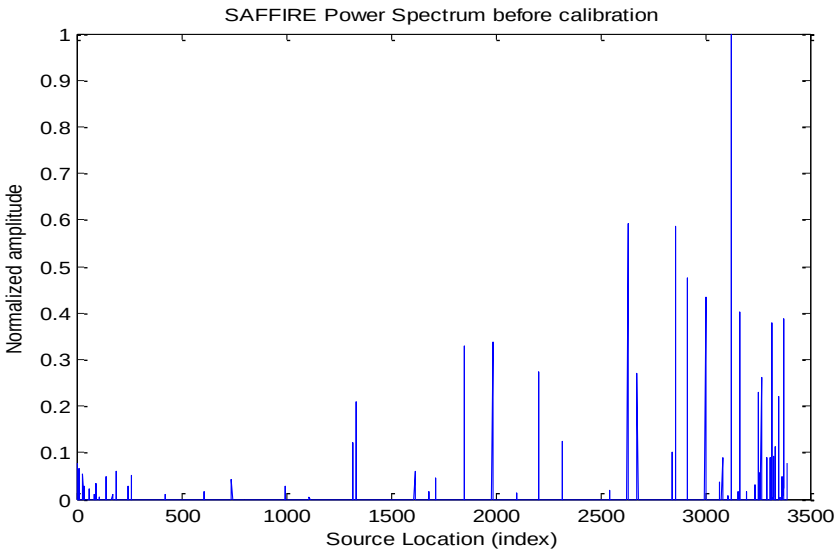

(a)

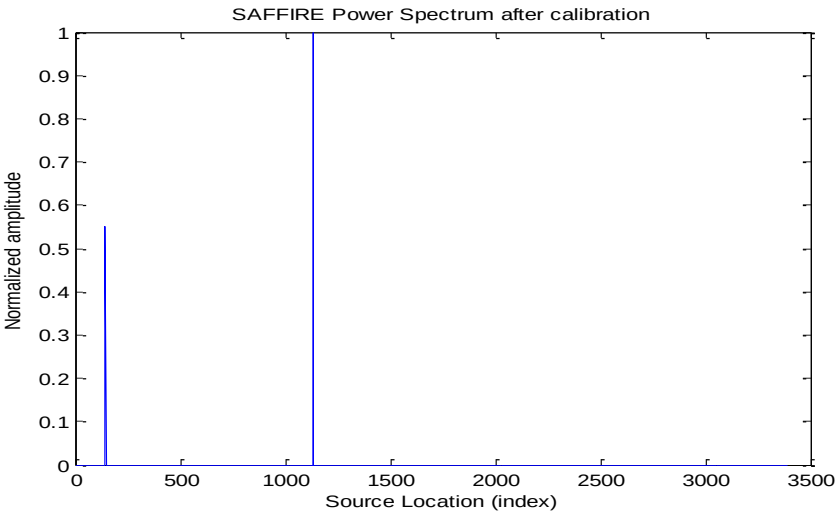

(b)

Figure 29: SAFFIRE power spectrum (a) before and (b) after calibration

In Fig. 30, the point that responds the most strongly to faces is plotted in red on the left of the cortex. The Talairach coordinates of the strongest point plotted on the magnetic resonance image (MRI), are x=-25, y=-39 and z=-21, which is similar to the left FFA described in [38]. The coordinates defined in [38] are x= -37 ± 4, y= –42 ± 7 and z=–16 ± 5. Therefore, there is a difference of 8 mm in the x direction.

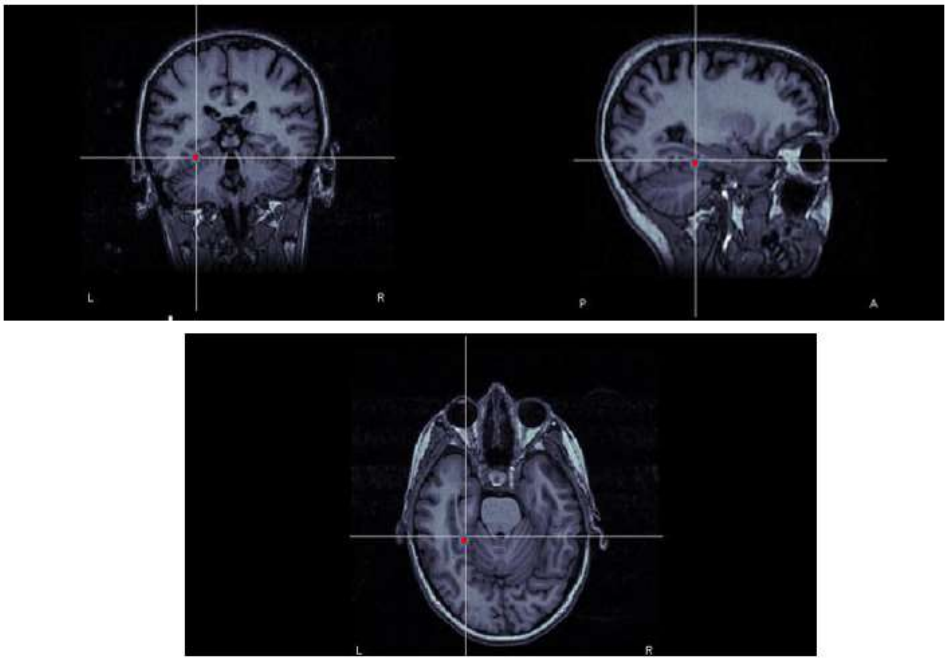

Figure 30: Realistic head MRI where the red point corresponds to the stronger source: Top left: coronal view, top right: sagittal view, bottom: axial view (Developed in Brainstorm)

Furthermore, the source amplitude estimate, obtained within a few iterations after applying the algorithm, is shown in Fig 31. This signal amplitude is found to be similar to the face identification event related potential (ERP) signal.

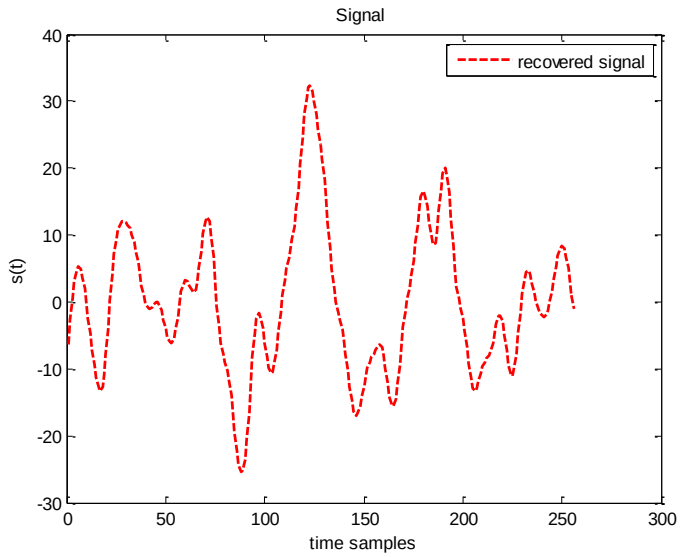

Figure 31: Stronger red source amplitude estimate- after calibration

The relatively weaker source plotted in blue in Fig.28 is located in the dorsal stream. Essentially, the dorsal stream terminates in the parietal lobe and is involved

with processing the object's spatial location relevant to the viewer. Although, it is not directly involved in the process of recognizing faces, it is involved in the guidance of actions and recognizing where objects are in space and is a part of the visual recognition process [39]. The corresponding source signal estimated using the Minimum Variance Beamformer (MVB) is illustrated in Fig.32.

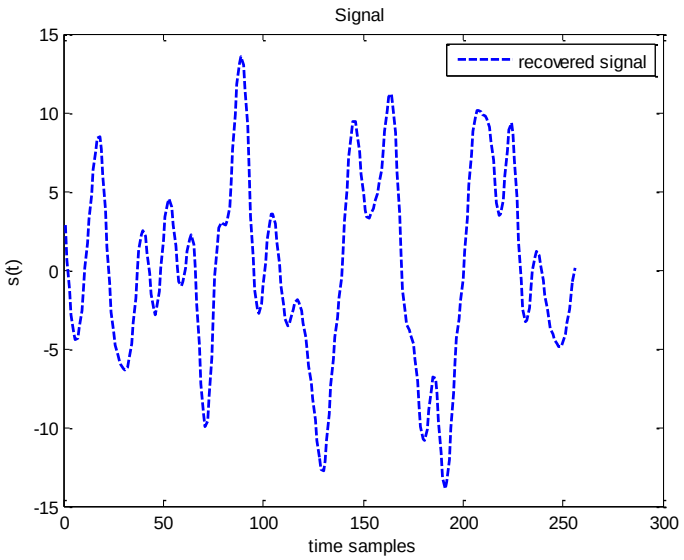

Figure 32: Weaker blue source amplitude estimate- after calibration

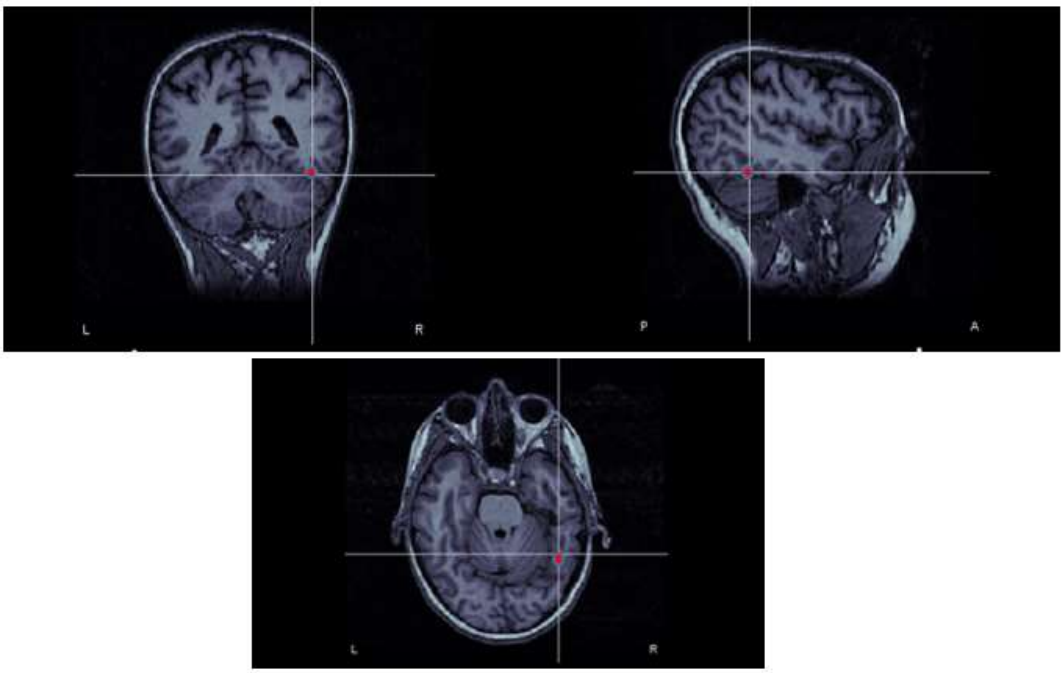

Figure 33: Realistic head MRI where the red point corresponds to the stronger source: Top left: coronal view, top right: sagittal view, bottom: axial view (Developed in Brainstorm)

Similarly, a small region of interest is selected on the right side of the cortex. The strongest source is mapped on the cortex, the MRI of which is provided in Fig.33. The Talairach coordinates of the strongest source plotted on the MRI are x=42, y=-48 and z=-27, which is similar to the right FFA described in [38]. The coordinates defined in [38] are 39 ± 3, –40 ±7, –16 ± 5. Therefore, there is a difference of 1 mm in the y direction and 6 mm in the z direction, corresponding to a total error of 7 mm.

Furthermore, the source amplitude, corresponding to the strongest source, is shown in Fig.34. This signal is found to be similar to the face recognition ERP signal and is recovered using the MVB technique that is a part of the proposed algorithm.

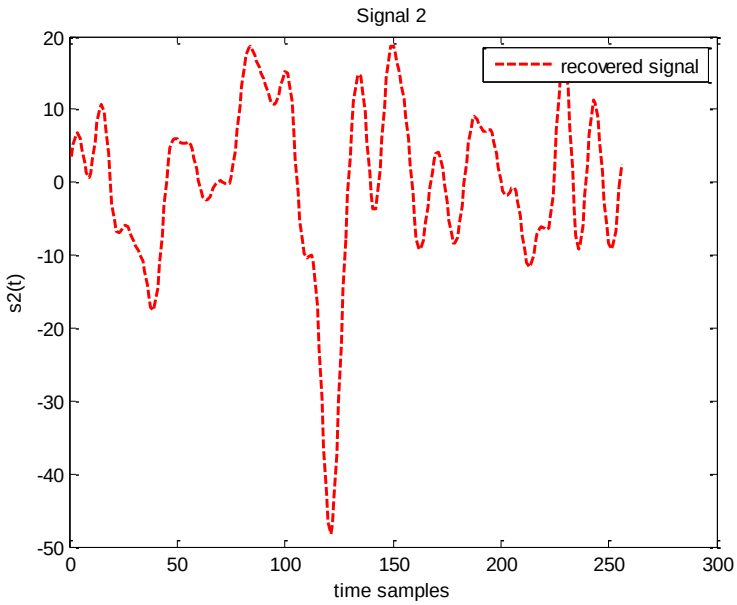

Figure 34: Strong source amplitude estimate- after calibration

The above figures validate that the algorithm is able to localize a strong source in the FFA region with a very small error. The algorithm is able to do this without having exact knowledge about the leadfield matrix of the head model for which the EEG signal was measured. Moreover, since source activation is anticipated in the FFA based on the experiment, the region of interest is chosen accordingly.

Chapter 8: Non-Stationary EEG Signal

As mentioned earlier in this thesis, the only way to localize the putative sources of neural activity in the brain is by making a-priori assumptions on the generation of the EEG signals. This is known as the *inverse problem.*

In Chapters 5, 6 and 7, EEG sources are assumed to be stationary over a certain period of time (static scenario). However, neural activity has strong temporal and spatial dynamics, since the EEG time scale is on the order of 100 milliseconds whereas that of an action potential is about 1 millisecond, thus giving rise to non-stationarity [3]. Therefore, in order to solve the inverse problem accurately, these dynamics must be taken into consideration.

In this chapter, a non-stationary EEG source reconstruction technique is incorporated as a part of the algorithm discussed in Chapter 6.

8.1 Taylor Series Expanded Beamformer (TBF)

Consider the received EEG signal measurement obtained from an array of *M* sensors for *N* time samples and *K* sources:

$$\boldsymbol{y}(n) = \boldsymbol{S}(n)\boldsymbol{x}(n) + \boldsymbol{v}(n) \tag{74}$$

$\boldsymbol{x}(n)$ is a *K x 1* vector of source amplitudes, $\boldsymbol{S}$ is an *M x K* normalized leadfield matrix which may vary with time and $\boldsymbol{v}(n)$ is the zero mean additive Gaussian noise. As mentioned in Section 6.2, a beamformer estimates the source signal as:

$$\boldsymbol{x}_k = \boldsymbol{h}_k{}^{\boldsymbol{T}}\, \boldsymbol{y}_k \tag{75}$$

where $\boldsymbol{h}$ is the weight vector. Expanding the weight vector in (75) using the first order Taylor series expansion, we obtain the source estimate to be:

$$\boldsymbol{x}_k = (\boldsymbol{h}_{ko} + (k - ko)\, \boldsymbol{h}'_{ko})^T\, \boldsymbol{y}_k \tag{76}$$

where, ko is the point of expansion. In matrix form, (76) can be represented as:

$$\boldsymbol{x}_k = \begin{bmatrix} \boldsymbol{h}_{ko} \\ \boldsymbol{h}'_{ko} \end{bmatrix}^T \begin{bmatrix} \boldsymbol{y}_k \\ (k - ko)\boldsymbol{y}_k \end{bmatrix} \tag{77}$$

In simpler notation,

$$\boldsymbol{x}_k = \boldsymbol{h}_{\boldsymbol{E}}{}^{\boldsymbol{T}}\, \boldsymbol{y}_{\boldsymbol{E}} \tag{78}$$

Similar to the Minimum Variance Beamformer (MVB) described in Section 6.2, we can mathematically express the problem as:

$$minimize \ \boldsymbol{h_E}^{\boldsymbol{T}} \boldsymbol{R_E} \boldsymbol{h_E}$$

$$subject\ to\ \boldsymbol{h_E}^{\boldsymbol{T}} \boldsymbol{S_E} = \mathbf{1} \tag{79}$$

where $\boldsymbol{h}$ is the weight vector and $\boldsymbol{R_E}$ is the covariance of the appended received signal $\boldsymbol{y_E}$. Furthermore, the steering vector $\boldsymbol{S_E}$ is described as:

$$\boldsymbol{S_E} = \begin{bmatrix} \boldsymbol{S} \\ 0_{Nx1} \end{bmatrix} \tag{80}$$

We obtain analytical solution to (79) by using the Lagrange multiplier method as:

$$\boldsymbol{h_E} = \boldsymbol{R_E}^{-1} \boldsymbol{S_E} \tag{81}$$

Thus, the expanded weight vector is useful in tracking the non-stationary signal of interest.

8.2 Results

The forward problem solution in this thesis was obtained using the Brainstorm software. A boundary element method (BEM) head model is used and the head model computations have been done on a realistic head anatomy with a resolution of 4 mm, which is a magnetic resonance imaging (MRI) volume provided by the French public research institute INRIA [15]. Next, experimental data is manipulated to form a realistic non-stationary EEG source signal. The modeled leadfield is obtained from Brainstorm and the perturbed measured leadfield is modeled as in (72). The algorithm was applied to the region of interest comprising of 1280 vertices on the brain and tested on the EEG signal consisting of 2 sources with 8% perturbation and 128 time samples.

As before, the SAFFIRE algorithm was applied in order to locate the sources with the largest peaks. The corresponding steering vectors (columns of the leadfield matrix) were then obtained and applied to the Taylor series expanded beamformer algorithm in order to estimate the source amplitudes. Finally, the estimated EEG signal was reconstructed and compared to the actual received signal via a calibration matrix. This procedure was repeated until a certain convergence criteria was met.

Fig.35 shows an example at an SNR of 20 dB, after the algorithm is applied to the Adaptive Beamformer (ABF). The ABF has a weight vector:

$$\boldsymbol{h}_{ABF} = \boldsymbol{R}^{-1}\boldsymbol{S} \tag{82}$$

where $\boldsymbol{R}$ is the covariance of the received signal $\boldsymbol{y}$. The ABF evidently is unable to accurately recover the amplitudes, especially for source 2.

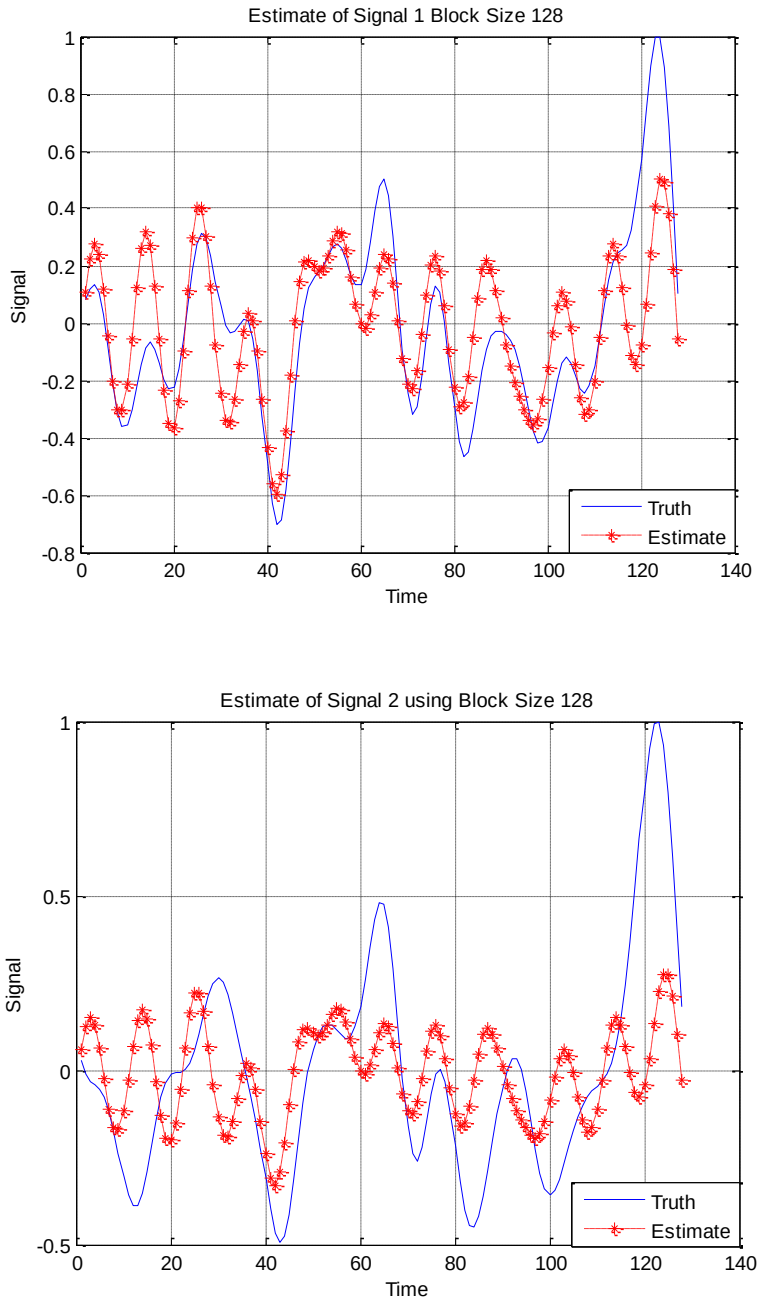

Figure 35: Normalized recovered source amplitude estimates 1 and 2 using ABF

Likewise, Fig.36 shows an example of the TBF at an SNR of 20 dB. After the proposed algorithm is applied, within a few iterations the estimated source 1 and source 2 amplitude is recovered for the TBF.

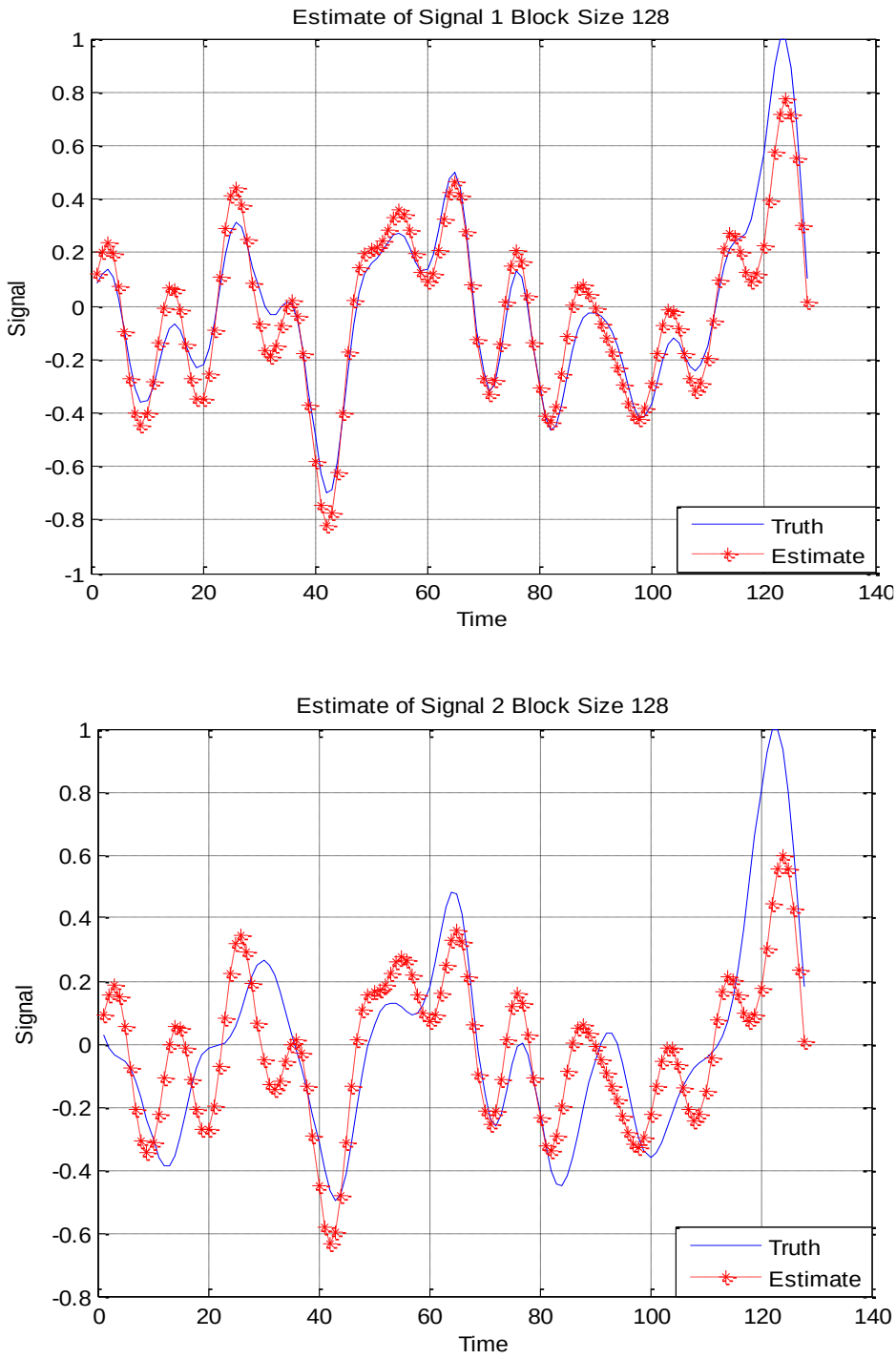

Figure 36: Normalized recovered source amplitude estimates 1 and 2 using TBF

As seen from the above figures it is clear that TBF recovers the source amplitudes with higher accuracy when compared to the ABF for both source 1 and 2.

The mean squared error (MSE) of the source signals, after calibration, is also shown in Fig.37, for various SNR. Fig.37 compares the source signal mean squared error obtained by averaging over 50 realizations of the Taylor series expanded beamformer and the adaptive beamformer.

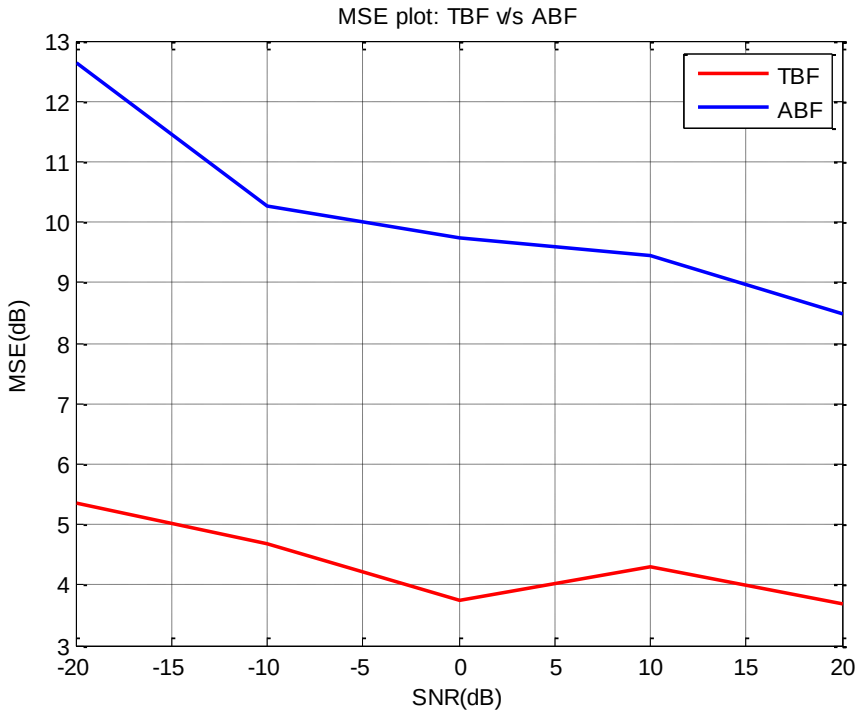

Figure 37: Comparative evaluation of the source amplitude MSE achieved by TBF and ABF

At an SNR of -20 dB the ABF has a source amplitude MSE of 12.1731 dB whereas TBF yields an MSE of 5.026 dB. This trend continues as the SNR increases from -20 dB to 20 dB. Therefore, the above figure illustrates that TBF is better suited for source amplitude recovery than ABF for all SNR.

Additionally, Fig.38 represents the localization error before and after calibration, where a threshold was applied in order to identify the strongest peaks as the recovered sources. The locations of the recovered test sources were compared to the ideal locations (in this case 165 and 285) at each iteration. In this simulation setup the algorithm stops when the localization error falls below a certain threshold.

The localization error was found by averaging over 150 iterations of the algorithm for each SNR with 20 percent perturbation in the leadfield matrix.

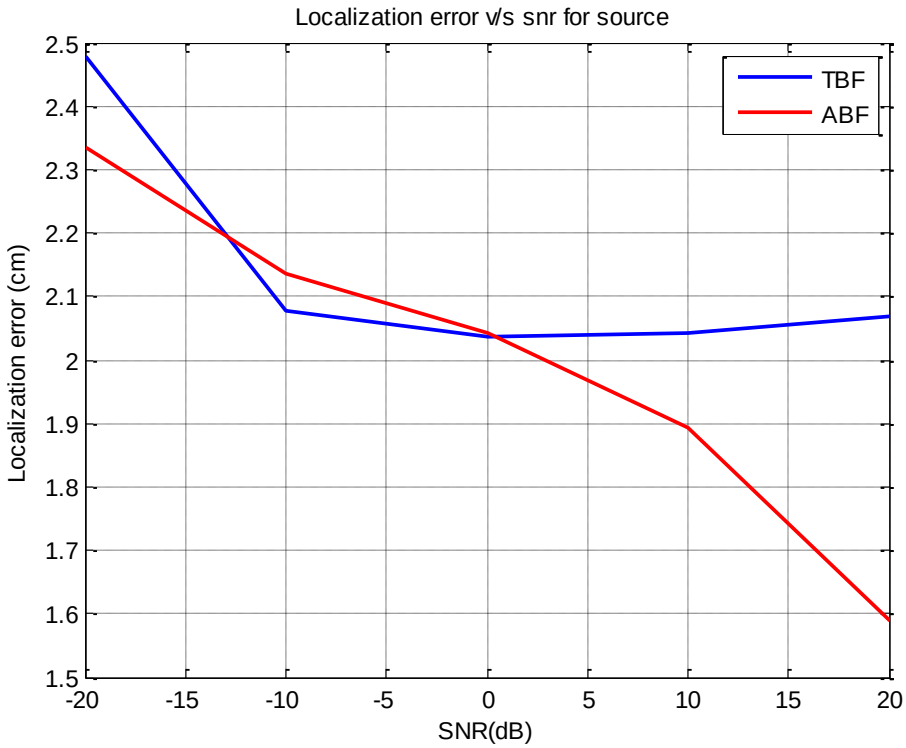

Figure 38: Average localization error (cm) for source 1 v/s SNR (dB)

The localization error for source 1 at an SNR of 20 dB, when the proposed algorithm in conjunction with TBF, is applied is found to be 2.4789 cm whereas with the ABF is 2.3824 cm. Moreover, from -15 dB to 0 dB ABF provides lower localization error than the TBF. However, at a higher SNR, ABF provides lower localization than TBF.

In conclusion, the difference in the MSE of the source amplitudes between TBF and ABF is much larger, where TBF recovers the amplitudes of the sources with lower error. In terms of the localization error, the difference between the two algorithms is comparable. As such, the Taylor Series Beamformer (TBF) is better suited to track the non-stationary EEG source position and determine its amplitude and must be employed as a part of the iterative algorithm proposed in Chapter 6.

Chapter 9: Conclusion

9.1 Conclusion

In this thesis, the performance of G-MUSIC and MUSIC was compared in the presence of leadfield perturbations when limited EEG sample size is available. G-MUSIC is based on G-estimation techniques and is a form of weighted MUSIC that performs better in scenarios where only limited sample support is available. Additionally, transfer function based external and auto calibration algorithms, were applied in order to account for the perturbations. The least squares calibration algorithm minimizes the distance between the modeled and measured leadfields, and the beamsum calibration algorithm adds an additional degree of freedom by projecting the modeled leadfield onto the measured leadfield. Results suggest that G-MUSIC yields lower MSE and localization error than least squares external and auto calibration techniques applied to MUSIC even when the applied perturbation is very small. Moreover, G-MUSIC coupled with external least squares is superior to its autocalibration counterpart. However, autocalibration only requires nominal source location estimate and thus is a more practical solution when compared to external calibration. The same pattern is observed when comparing external and auto beamsum calibration. Results also illustrate that G-MUSIC with beamsum autocalibration provides lower localization error than least squares autocalibration in low SNR environments.

Furthermore, an iterative algorithm is developed in this thesis for the purpose of EEG source localization. This algorithm addresses the problem of localization when exact knowledge of the leadfield matrix is not available. A calibration technique is implemented in order to localize the sources of neural activity and to determine their amplitudes. Therefore, a realistic scenario is simulated where both the locations and the amplitudes of the sources are estimated with good accuracy. Furthermore, the algorithm was tested on experimental data in order to localize areas of the brain activated during the facial recognition process. The strongest sources were mapped on the left and right FFA with a small error, validating the performance of the algorithm.

The final part of the thesis deals with non-stationary EEG signals. The developed iterative algorithm is applied to the non-stationary signal. However, the minimum variance beamformer in the algorithm is replaced by the Taylor series

expanded beamformer, in order to track the source amplitudes. The performance of this beamformer is compared to the Adaptive Beamformer (ABF) in terms of the localization error and source amplitude MSE. Compared to the adaptive beamformer, the Taylor Beamformer (TBF) provides lower MSE, however, its localization error is comparable to that of the ABF. Nevertheless, since the difference in MSE is very large between the two algorithms, it is more suitable to employ the TBF as a part of the proposed algorithm in order to track the non-stationary EEG source signal.

However, as mentioned earlier this algorithm works best when the initial assumption regarding the source location and amplitudes are close to the actual values; therefore, the region of interest must be chosen accordingly.

9.2 Future Work

The work in this thesis can be extended in various ways. Although the algorithm developed in this thesis is applied on a realistic head model using BEM head model computations, the assumed head model is isotropic. Therefore, the performance of this algorithm could be tested on head models that take into account the inhomogeneity and anisotropy of the head using FEM based methods.

Furthermore, this thesis assumes the orientation of the dipole to be normal to the surface of the cortex which is physiologically justified, however this algorithm can be tested in a scenario where this restriction is not imposed on the orientation of the source dipole model. Moreover, localization of neural activity is assumed to be originating from the cortex since it contains most of the neurons. Nevertheless, deeper structures of the brain, such as the cerebellum, also contribute to the recorded potentials on the scalp. Localizing these deeper sources of activity could be beneficial in further understanding the brain functions. Another active area of research is focusing more on the relationship (correlation) between brain sources in different brain locations as a response to a certain type of stimuli.

Finally, another exciting issue in brain source localization is combining the data obtained from different modalities. Since, EEG provides good temporal resolution and fMRI provides excellent spatial resolution, the data could be integrated in order to provide insight that could not be achieved with either imaging technique alone.

References

[1] C. M. Michel, M. M. Murray, G. Lantz, S. Gonzalez, L. Spinelli, and R. Peralta, "EEG source imaging," *Clinical Neurophysiology*, vol. 115, no. 10, pp 2195-2222, Oct 2004.

[2] J.C. Mosher and R.M. Leahy, "Source localization using recursively applied and projected (RAP) MUSIC," *IEEE Transactions on Signal Processing*, vol. 47, no.2, pp. 332-340, 1999.

[3] P.P. Indic, R.R. Pratap, V.N. Nampoori, and N.N. Pradhan, "Significance of Time Scales in Nonlinear Dynamical Analysis of EEG Signals," *International Journal of Neuroscience*, vol.99, no.1-4, pp. 181, Aug. 1999.

[4] X. Mestre, "An improved weighted MUSIC algorithm for small sample size scenarios," *in Proceedings of Adaptive Sensor Array Processing Workshop*, 2006.

[5] T. Zarghami, H.S. Mir, and H.Nashash, "Calibration of Low Density EEG Sensor Arrays for Brain Source Localization," *Proceedings of 2013 International Conference on Neural Information Processing*, pp. 331 - 338, Nov. 2012.

[6] H.S. Mir, J.D. Sahr, G.F. Hatke, and C.M. Keller, " Passive direction finding using an airborne sensor array in the presence of manifold perturbations," *IEEE Transactions on Signal Proces*sing, vol. 55, no.1, pp. 2486-2496, Jan. 2007.

[7] M.Teplan, "Fundamentals of EEG measurement," *Measurement Science Review*, vol.2, no.2, pp1-11, 2002.

[8] L. O. Tanzer, "Numerical modeling in electro and magneto encephalography," Ph.D. dissertation, Dept. Eng. Physics and Math., Biomedical Eng. Lab., Helsinki Univ. of Technology, Espoo, Finland, 2006.

[9] "Brain Structures and their Functions," in *Serendip Studio* [Online], Available: http://serendip.brynmawr.edu/bb/kinser/Structure1.html, [15 July 2014].

[10] "Brain and Nervous System Health Center," in *WebMD* [Online], Available: http://www.webmd.com/brain/picture-of-the-brain, [15 July 2014].

[11] "Communication between neurons," in *Educarer* [Online], Available: http://www.urbanchildinstitute.org/why-0-3/baby-and-brain, [15 July 2014].

[12] C. Burdusel, "Basic facts about neurons," *The Australasian Journal of Neuroscience*, vol.17, no.2, pp. 9-12. 2006.

[13] "Action Potential," in *Wikipedia* [Online], Available: http: / / sv. wikipedia .org / wiki / Aktionspotential , [15 July 2014].

[14] "The Neuron," in *General Psychology* [Online], Available: http: / / webspace.ship.edu / cgboer / theneuron.html , [15 July 2014].

[15] S. Baillet, J.C. Mosher, and R.M. Leahy, "Electromagnetic brain mapping," *IEEE Signal Process*ing *Magazine*, vol. 18, no. 6, pp 14-30, Nov. 2001.

[16] "Brain Computer Interfacing," [Online slides], Available: http : / / yosinski.com / mlss12 / MLSS-2012-Muller-Brain-Computer-Interfacing / , [17 July 2014].

[17] D.W. Penny, and K.J. Friston, "Functional imaging," in *Scholarpedia*, vol. 2, no.5, pp 1478, 2007.

[18] E.Z. Golumbic, "What is EEG?" [Online article], Available: https : / / www.mada.org.il / brain / articles / faces-e.pdf, [17 July 2014].

[19] M. Hämäläinen, H. Riitta, R.J. Ilmoniemi, J. Knuutila, and O.V. Lounasmaa, "Magneto- encephalography—theory, instrumentation, and applications to noninvasive studies of the working human brain." *Reviews of modern Physics*, vol. 65, no. 2, pp 413-497, 1993.

[20] F.T. Ulaby, E. Michielssen, and U. Ravaioli, *Fundamentals of Applied Electromagnetics*, Upper Saddle River, NJ: Prentice Hall, 2010.

[21] "Modeling and Inverse Problems in EEG/MEG," in *Applied Mathematics Munster* [Online slides], Available: http://imaging.uni-muenster.de/research/eeg_meg/ , [1 August 2014].

[22] J.T. Cacioppo, L.G. Tassinary, and G.G. Berntson, *Handbook of Psychology*, NY: Cambridge University Press, 2007.

[23] D. Cheyne and J. Verba, "Biomagnetism" in *Encyclopedia of Medical Devices and Instrumentation*, Hoboken, N.J.: Wiley-Interscience, 2006.

[24] R. Grech, T. Cassar, J. Muscat, K. P. Camilleri, S.G. Fabri, M. Zervakis, P. Xanthopoulos, V. Sakkalis, and B. Vanrumste, "Review on solving the inverse problem in EEG source analysis*," Journal of Neuroengineering and Rehabilitation*, vol. 5, no. 25, Nov.2008.

[25] F. Luan, C. Lee, J. Choi, and H. Jung, "A comparison of regularization techniques for magnetoencephalography source reconstruction," *IEEE Transactions on Magnetics*, vol. 46, pp.3209 - 3212, Aug. 2010.

[26] J. Foutz, A. Spanias, and M. K. Banavar, *Narrowband Direction of Arrival Estimation for Antenna Arrays*, Morgan and Claypool Publishers, 2008.

[27] "Ultrasonic Inspection – Near Field Calculation," [Online document], Available:http://www.ndt-ed.org/GeneralResources/Formula/UTFormula/near_field/near.html, [1 August 2014].

[28] B. Yvert, A. Croizeix-Chelys, and J. Bernier, "Fast realistic modeling in bio electromagnetism using lead-field interpolation", *Human Brain Mapping*, vol. 14, no.1, pp. 48-63, Sep 2001.

[29] Z.A.Acar and S. Makeig, “Effects of Forward Model Errors on EEG Source Localization,” *Brain Topography*, vol 26, no.3, pp.378-396, July 2013.

[30] D. Weinstein, L. Zhukov, and C. Johnson, “Lead field basis for FEM source localization,” *Technical report, Department of computer science*, University of Utah, 1999.

[31] M. Popescu, S.D. Blunt, and T. Chan, "Magnetoencephalography Source Localization using the Source Affine Image Reconstruction (SAFFIRE) Algorithm," *IEEE Transactions on Biomedical Engineering*, vol. 57, no.7, pp. 1652-1662, July 2010.

[32] S. D. Blunt, T. Chan, and K. Gerlach, “Robust DOA estimation: The reiterative super resolution (RISR) algorithm,” *IEEE Transactions on Aerospace and Electronic Systems*, vol. 47, no.1, pp. 332–346, Jan. 2011.

[33] C. Lederman, A.A. Joshi, I.D. Dinov, J.D. Van Horn, L.A.Vese, and A.W. Toga, “Tetrahedral mesh generation for medical images with multiple regions using active surfaces,” *Proceedings of IEEE International Symposium on Biomedical Imaging*, pp. 436–439, 2010.

[34] R. Lorenz and S. Boyd, “Robust minimum variance beamforming,” *IEEE Transactions on Signal Processing*, vol. 53, no. 5, pp.1684-1696, 2005.

[35] T. Zarghami, H. Mir, and H. Al-Nashash, “Transfer Function Based Calibration of Sparse EEG Systems for Brain Source Localization," *IEEE Sensors Journal*, vol. 15, no.3, pp. 1504 - 1514, Mar. 2015.

[36] M.V. Peelen and P E. Downing, “Selectivity for the human body in the Fusiform Gyrus,” J*ournal of Neurophysiology*, vol. 93, no**.** 1, pp. 603-608, Jan 2005.

[37] G. Iaria, C.J. Fox, C. Waite, I. Aharon, and J.J.S. Barton, “The contribution of the fusiform gyrus and superior temporal sulcus in processing facial attractiveness: Neuropsychological and neuroimaging evidence,” *Neuroscience*, vol. 155, no.2, pp 409- 422, Aug 2008.

[38] K. Grill-Spector, N. Knouf, and N. Kanwisher, “The fusiform face area subserves face perception, not generic with-in category identification, ”*Nature Neuroscience*, vol. 7, no. 5, pp. 555–562, 2004.

[39] A. Martinez, N. Revheim, P.D. Butler, D.N. Guilfoyle, E.C. Dias, and D.C. Javitt, “Impaired magnocellular/dorsal stream activation predicts impaired reading ability in schizophrenia,” *NeuroImage: Clinical*, vol. 2, pp. 8–16, 2013.

[40] M.S. Amin, M.R. Azim, S.P.Rahman, M.F. Habib, and M.A. Hoque, “Estimation of Direction of Arrival (DOA) Using Real- Time Array Signal Processing and Performance Analysis,” *International Journal of Computer Science and Network Security*, vol. 10, no. 7, July 2010.

[41] J.J. Ermer, J.C. Mosher, S. Baillet, and R.M. Leahy, “Rapidly recomputable EEG forward models for realistic head shapes,” *Physics in Medicine and Biology*, vol. 46, no. 4, pp 1265-1281, Apr. 2001.

[42] F. Tadel, S. Baillet, J.C. Mosher, D. Pantazis, and R.M. Leahy, "Brainstorm: A User-Friendly Application for MEG/EEG Analysis," *Computational Intelligence and Neuroscience*, vol.2011, pp.1-13, 2011.

[43] R. Couillet and M. Debbah, "Signal Processing in Large Systems: a New Paradigm," *IEEE Signal Processing Magazine*, vol.30, no.1, pp. 24-39, 2013.

[44] Y. Zhang, W. van Drongelen, and B. He, "Estimation of *in vivo* brain-to-skull conductivity ratio in humans," *Applied Physics Letters*, vol. 89, no.22, 2006.

[45] A. Khabbazibasmenj, S.A. Vorobyov, and A. Hassanien, "Robust Adaptive Beamforming Based on Steering Vector Estimation With as Little as Possible Prior Information," *IEEE Transactions on Signal Processing*, vol.60, no.6, pp. 2974-2987, June 2012.

Vita

Rabiya Nakhat Momin was born in 1991, in Sharjah, United Arab Emirates. She graduated from The Indian High School in Dubai in 2009. Ms. Momin joined the American University of Sharjah in 2009 and graduated in the year 2013 with a Bachelor's degree in Electrical Engineering. She was granted a teaching assistantship in order to pursue a Master's program in Electrical Engineering at the American University of Sharjah. Ms. Momin is a member of the IEEE Engineering in Medicine and Biology Society (EMBS) and has published a paper in the 36th EMBC conference held in Chicago, USA.